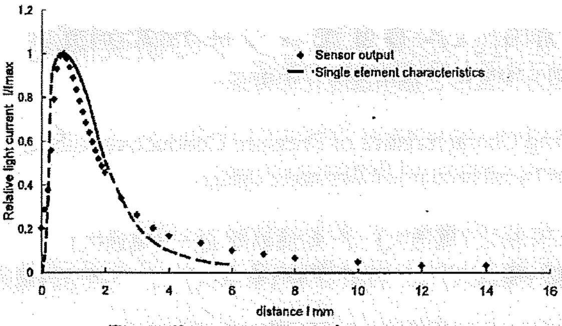

Fig.6 Distance output characteristics

素子の持つ指向性から，遠距離ではその影響が相対的に大きくなるためだと推測できる．この性質については，対象物体表面での反射・散乱などを考慮した光学的な側面からの考察を同時に行っている．

5. センサシートの試作

提案する設計手法について妥当性の確認ができたため，次にフレキシブル基板を用いて提案するセンサシートの試作を行った．さらに，ハーモニック・ドライブ・システムズ社製3指ロボットハンド（図7）への取り付けのため，長さ40×幅25×厚さ20[mm]先端R=15[mm]の指先部材（硬質ポリウレタン製）の表面に貼り付けた．その概観を図8に示す．

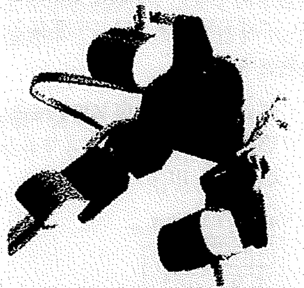

Fig.7 Overview of the robot hand

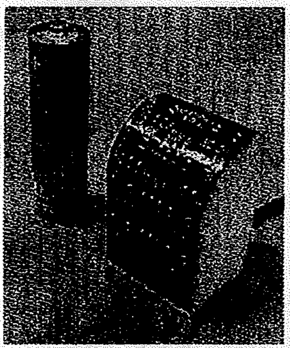

Fig.8 the Prototype of fingertip

6. 特性評価

試作したセンサ付指先について，位置・距離検出特性の評価試験を行った．Kodak 90% グレーカードに対し，1軸回転ステージ上に取り付けた指先を正対させ，仰角と距離を変化させたときの各出力の変化は図9，図10となった．

位置出力については距離5[mm]以降でほぼ角度に応じて一定の値を示している．その一方で，距離出力は角度変化の影響を受けて2倍近く変動してしまっている．仰角0[deg]で位置出力が-0.5付近を示していることと合わせると，この特徴は今回の指先形状と素子配置では検出対象物に正対するセンサ素子の個数が変化することに起因すると考えられる．

この距離出力の変動については，素子配置の最適化や，センサ出力取り込み後に位置出力を元にして補正を行うことなどによる改善を考えている．

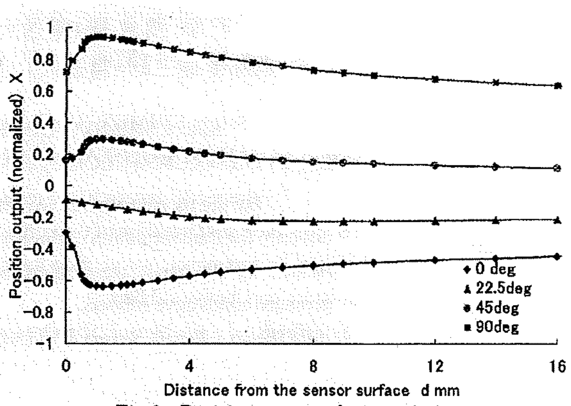

Fig.9 Position output characteristics

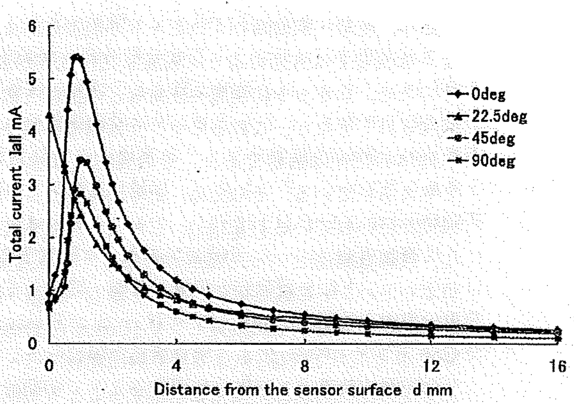

Fig.10 Distance output characteristics

7. 結言

ロボットハンド指先への搭載を目指し，ネット状近接覚センサの小型・薄型化のための設計を行った．表面実装型のフォトインタラプタを用いて，4素子×2列に配置した場合について回路動作の解析と設計を行った．その結果を基にフレキシブル基板を用いたネット状近接覚センサシートを試作し，指先表面に装着時の検出特性の評価を行った．

今後は，ハンドシステムとの統合を行い，指と対象物との位置関係情報を利用した高速かつ確実な把持動作の実装を予定している．

参考文献

[1] 溝口ほか: "インテリジェントロボットハンドの研究開発", 第26回日本ロボット学会学術講演会'08 講演論文集, 2008.

[2] 天本, 下条: "2次元状に配置した近接覚センサによる対象物の中心位置検出方式", 第24回日本ロボット学会学術講演会'06 講演論文集, 2006.

[3] 長谷川ほか: "ロボットハンド指先に搭載可能な薄型ネット状近接覚センサシートの開発", 第9回計測自動制御学会システムインテグレーション部門講演会 講演論文集, 2008.

2P1-J13

感圧導電性ゴムの特性を用いた滑り覚センサの研究開発

—法線および接線方向変形と抵抗値変化の関係—

High Sensitivity Slip Sensor utilizing Characteristics of Pressure Conductive Rubber

-Relationship between Transformation and Resistance change-

○学 清水 智 (電通大)　綿奈部 裕之 (電通大) 学 勅使河原 誠一 (電通大)
正 多田隈 建二郎 (電通大) 正 明 愛国 (電通大) 正 石川 正俊 (東京大) 正 下条 誠 (電通大)

Satoru SHIMIZU(UEC),Hiroyuki WATANABE(UEC),Seiichi TESHIGAWARA(UEC),
Kenjiro TADAKUMA(UEC),Aiguo MING(UEC),Masatoshi ISHIKAWA(Tokyo Univ.),Makoto SHIMOJO(UEC)

By the recent research, we found that the electrical resistance change occurs when the transformation of not only the transformation of the normal direction but also the shear direction occurred to the pressure conductive rubber. In this paper, we verified the characteristic to the normal force and the tangential force about various pressure conductive rubbers.

Key Words : *Tactile Sensor, Slip Detection, Pressure Conductive Rubber*

1. はじめに

近年，産業・家庭問わずロボットの需要が高まっており，そのような現場では人間のように高度な把持動作が要求されている．そのため，ロボットに視覚や圧覚などの情報を取得するセンサが開発されてきたが，これらのセンサは摩擦係数や重量が未知である物体の把持は困難であり，その実現には滑り覚が重要であると考えられている．そのため，近年滑り覚センサに関する様々な研究が行われている [1][2][3]．しかし，これらは省配線性，小型化，複雑な構造といった問題点がある．本研究室ではこれまで，ロボットハンドに装着可能な柔軟・薄型・軽量・省配線の 2 次元荷重分布中心位置検出触覚センサ (Center of Pressure センサ，以降 CoP センサと呼ぶ) による滑り検出実験を行っており，CoP センサの特徴的荷重出力変化を利用することで初期滑りの検出が可能であることを示している [4]．また，この変化は CoP センサに用いられている感圧導電性ゴムの抵抗値変化に起因することがわかっている [5][6]．感圧導電性ゴムは，ゴム内部の導電粒子形状や充填量により様々な種類・感度が得られる．しかし，これらの違いによる特性の変化に関する検討はなされていなかった．そこで本稿では，感圧導電性ゴムの種類や感度の異なる感圧導電性ゴムについて法線方向力・接線方向力を与えたときの感圧導電性ゴムの抵抗値特性を検証する．まず 2 章では，本実験で用いる滑り検出部と感圧導電性ゴムについて述べる．3 章では，感圧導電性ゴムに対し法線方向力を付加した時の特性について述べる．4 章では，感圧導電性ゴムにせん断力を付加した時の特性について述べる．5 章では，本実験で得られた知見についてまとめる．

2. 実験準備および導電原理

2.1 滑り検出部の構成

電極は 2 つが互い違いに渦巻状に配置されており，この電極の上に感圧導電性ゴム ($6[mm] \times 6[mm] \times 0.5[mm]$) を設置し，滑り検出部を構成している．本センサは薄型かつ小型であり，自由曲面に配置することが可能という利点を持つ．本実験では電極を $1k\Omega$ の抵抗を介して安定化電源に接続し，$5V$ の電圧を印加した．そのため，電極間電圧は定常状態では $5V$ を示す．本実験では以下の 3 タイプの感圧導電性ゴムを用いた．また，感圧ゴム II については高感度タイプと中感度タイプの 2 種類を用意し，検証を行なった．

- 感圧ゴム I(板状導電粒子配合)
- 感圧ゴム II(針状＋ナノサイズ導電粒子)
- 感圧ゴム III

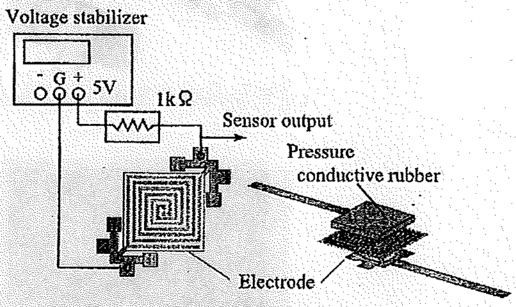

Fig.1 滑り検出部

2.2 感圧導電性ゴム

滑り検出部に用いられている感圧導電性ゴムは内部の導電粒子の分布状態，接触状態の変化により抵抗値が変化する．したがって，ゴムの厚み方向の変形以外に，せん断変形が生じた場合でも抵抗値変化が生じることが知られている [5]．Fig.2 にその模式図を示した．Fig.2-(a) は感圧導電性ゴムを渦巻き電極に設置した状態である．このように無加圧状態ではゴムの抵抗値は ∞ であり，電流は流れない．(b) のようにゴムの厚み方向に変形が起きると感圧導電性ゴムの抵抗値は減少し電流が流れる．さらに，(c) のように物体に滑りを発生させる外力 (f_t) が負荷されるとゴムにせん断変形 (γ_{xy}) が生じ，抵抗値が上昇する．

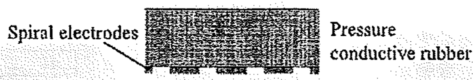

(a) Initial state

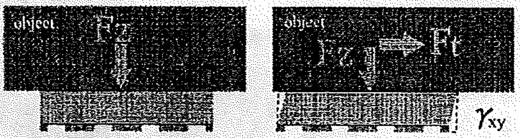

(b) Reduction of resistance (c) Resistance increase

Fig.2 感圧導電性ゴムの内部モデル

3. 法線方向力負荷実験

3.1 実験概要および方法

本実験で用いた実験装置を Fig.3 に示す．2.1 節にて構成した滑り検出部を加振器の直下に設置している．加振器を駆動することにより法線方向力の負荷と除荷を行い，加振器先端に装着されているロードセルによって加圧力を計測可能な構成となっている．また，加振器上部に設置されたレーザー変位計によりゴムの変形量を計測可能である．滑り検出部の上にはアクリルプレート (20[mm] × 20[mm] × 5[mm]) を置きゴム全体で加圧力を受ける構造となっている．また，加圧部の先端には曲率を設け，片当たりの影響を減少させる構造にした．

Fig.3 の実験装置を用い，法線方向荷重を与えた時の感圧導電性ゴムの抵抗値変化を電圧変化として計測する．サンプリング周期を 500[H_z] とし，加振器を 0.1[H_z] の周期で駆動し感圧導電性ゴムの厚み方向に 4 回の負荷と除荷を与えた．本実験では無加圧状態から感圧導電性ゴムの出力値が飽和するまでの範囲で加圧を行なった．また，1 回目の試行の後，6 時間の無加圧状態を設けて感圧導電性ゴムを十分回復させ 2 回目の試行を行なった．本実験により得られるデータは以下の通りである．

- 滑り検出部の出力変化 (ゴムの抵抗値変化)
- ロードセルの出力 (法線方向力)
- レーザー変位計の出力 (ゴムの変形量)

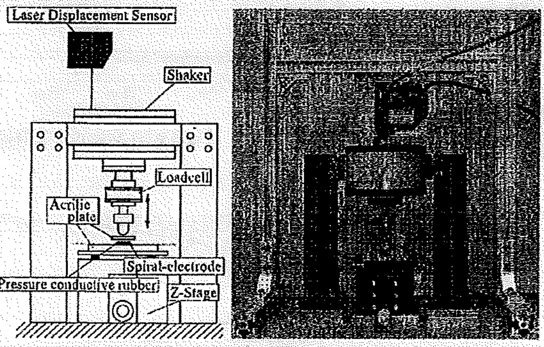

Fig.3 法線方向力負荷実験装置

3.2 結果

本実験の結果を Fig.4，Table 1 に示す．Fig.4 の縦軸は電極間電圧，横軸は加圧力である．Table 1 からわかるように，感圧導電性ゴムは内部の構造が異なっていたとしてもヒステリシス特性を有し，その大きさは感度・構造によって異なる事がわかった．また，今回の実験では感圧ゴム I(板状導電粒子配合タイプ) が最もヒステリシスが小さいという結果を得た．2 回目の試行を行なった結果を Fig.5 に示す．Fig.5 に示したように，2 回目の試行では 1 回目の試行で描いたヒステリシスループとは異なるヒステリシスループを描き，推移することがわかった．また，ヒステリシスループの推移は，今回用いたどの感圧導電性ゴムでも見られた．

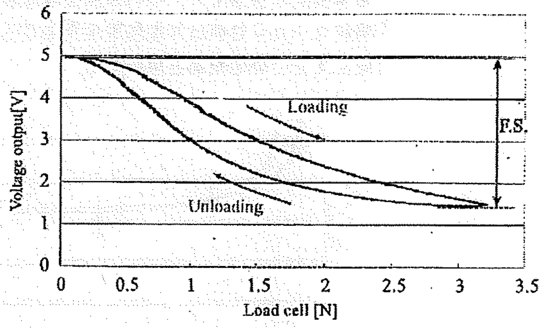

Fig.4 ヒステリシス特性

Table 1 ヒステリシス

	ヒステリシス [% $of F.S$]
感圧ゴム I	8.22
感圧ゴム II-高	24.5
感圧ゴム II-中	23.7
感圧ゴム III	18.3

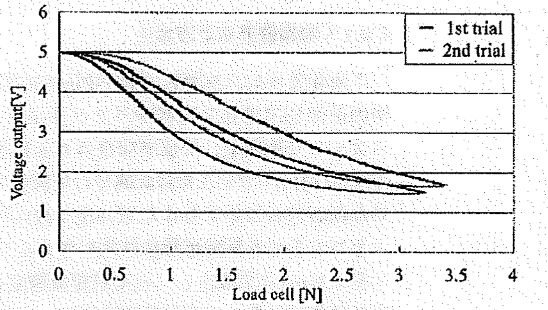

Fig.5 ヒステリシスループの推移

3.3 考察

Fig.4，Table 1 のように各感圧導電性ゴムでヒステリシスの大きさに違いが見られた．感圧導電性ゴムの主成分は粘弾性体であるゴム材料である為，その変形挙動は粘弾性特性を有する．そのため，しばしば解析モデルとしてバネーダンパモデルで表される．今回用いた感圧導電性ゴムは，各ゴムで内部の導電粒子形状やその充填量が異なるために変形の生じやすさ，つまり解析モデルで言うところの粘性係数や弾性係数が異なる為にヒステリシスの大きさに違いが現れたと考えられる．また，Table 1 の感圧ゴム II-高感度と中感度を比較すると，構造が同じ場合ではヒステリシスに大きな差異が見られない為，ヒステリシスの大きさに対し，より支配的な要因は導電粒子形状であると考えられる．

Fig.5 に示したように感圧導電性ゴムではヒステリシスループの推移が生じることがわかった．本実験では繰り返し荷重を与え

ていることから，この特性の発現要因は，加圧回数にあるのではないかと考えた．そこで，Fig.6 に与える繰り返し荷重の回数を変化させた実験を行なった結果を示す．Fig.6 の縦軸は初期計測時の電圧変化量 (ΔV_0) に対する加圧後の電圧変化量 (ΔV_n) の割合 ($\Delta V_n/\Delta V_0$)，横軸は加圧回数である．この結果から，ヒステリシスループの推移は加圧回数の増加に伴い 1 万回付近までは大きな変化を生じるが，それ以降では推移量が小さくなるという結果になった．これは，加圧を加えるごとにゴムの抵抗値変化が安定してきているためと思われる．

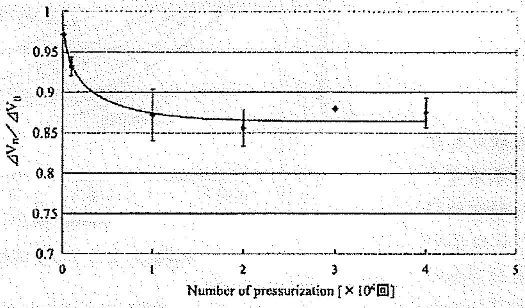

Fig.6 加圧回数による検証

4. せん断力付加実験

前章では，様々な種類の感圧導電性ゴムに対し法線方向力を付加した際の特性の違いについて検証を行なった．本章では，接線方向力を付加した際の特性の違いについて検証を行なう．

4.1 実験概要および方法

本実験で用いた実験装置を Fig.7 に示す．2. にて構成した滑り検出部を円で囲んだ右側のアクリルプレートに貼り付けた．X-ステージを駆動し，感圧導電性ゴムに法線方向力 (F_z) を加えた (Fig.7-(1))．次に，左側に配置した自動ステージを駆動し，ゴムにせん断方向の変形を与えた (Fig.7-(2))．また，レーザー変位計によりゴムのせん断変形量を計測できる．本実験ではせん断変形量を 0.3[mm] に固定し，せん断変位速度 ($\dot{\gamma}_s$) を 50 ~ 3000[$\mu m/s$] まで変化させた．本実験装置を用い，以下の項目について実験を行った．

- 種類の異なるゴムにせん断変形を与え，電極間電位を観察
- せん断変形量を一定とし，法線方向力・せん断速度を変化させた時の電圧変化量 ($\triangle V$) を測定

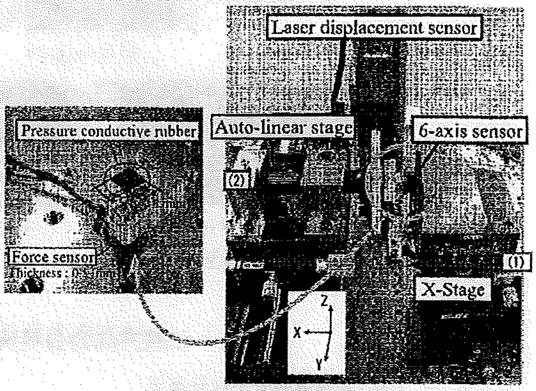

Fig.7 せん断力付加実験装置

4.2 結果

感圧ゴムにせん断変形を付加したときの電圧変化の様子を Fig.8 に，加えるせん断変形の速度を変えたときのせん断速度と電圧変化量の関係を Fig.9 に示す．Fig.9 の右側に示した数値は、電圧変化量の最大・最小値とその差である。同様に求めた各感圧導電性ゴムの構造による電圧変化量の違いを Table 2 に示す．

Fig.8 よりせん断変形を与えることによって電圧変化が大きい，せん断速度 ($\dot{\gamma}_s$) が大きいほど電圧変化量が大きくなることがわかる．また，Fig.9 より感圧導電性ゴムにせん断変形を与えたときの電圧変化 (ΔV) は，せん断速度 ($\dot{\gamma}_s$)，法線方向力 (F_z) に依存することがわかった．Table 2 に示したように，高感度タイプの方が電圧変化量 (ΔV) がより大きな値を示しており，高感度のもの程電圧変化を生じやすい事がわかる．

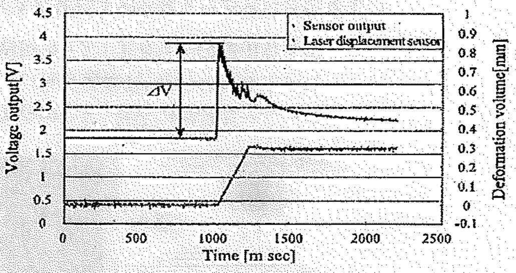

Fig.8 せん断力付加実験結果

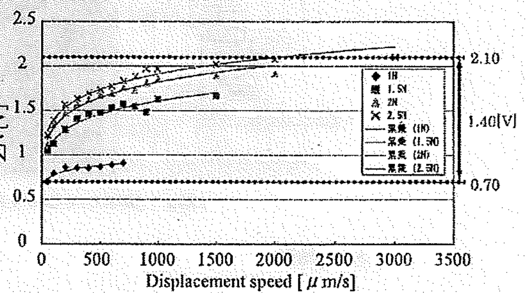

Fig.9 せん断速度 ($\dot{\gamma}_s$) と電圧変化量 ($\triangle V$) の関係

Table 2 電圧変化量の最大・最小とその差分

	Max[V]	Min[V]	Max-Min[V]
感圧ゴム I	1.03	0.35	0.68
感圧ゴム II-高	2.1	0.7	1.4
感圧ゴム II-中	0.56	0.94	0.38
感圧ゴム III	1.16	0.38	0.78

4.3 考察

これらの実験結果より，最小二乗法を用いて近似曲線の式を求め，関係式を導出した．以下に導出した関係式を示す

$$\Delta V = K \cdot \dot{\gamma}_s^n \qquad (1)$$

ここで係数 K と n それぞれについてと法線方向力 Fz との関係を検証した．

Fig.10 より係数 K と n は法線方向力 F_z の一次関数で近似できるとわかった．そこで係数 K と n を以下のように仮定した．

$$K(F_z) = aF_z + b \qquad (2)$$

$$n(F_z) = cF_z + d \qquad (3)$$

(2), (3) 式を代入する

$$\Delta V = (aF_z + b) \cdot \dot{\gamma}_s^{(cF_z+d)} \qquad (4)$$

(4) 式より電圧変化量 (ΔV) をせん断速度 ($\dot{\gamma}_s$) と法線方向力 (F_z) の関数であると示した．このことから，せん断力付加による感圧導電性ゴムの抵抗値変化は法線方向力 (F_z) とせん断速度 ($\dot{\gamma}_s$) の両方に依存すると考えられる．

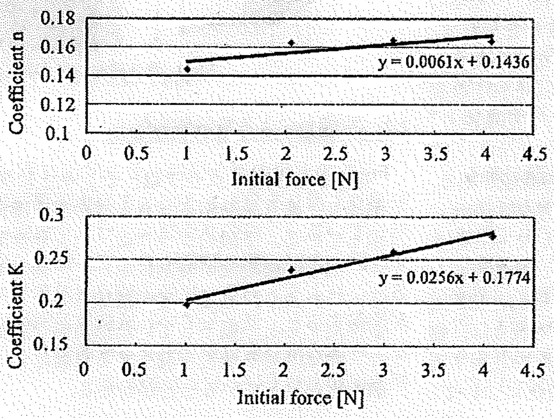

Fig.10 係数 K, n と法線方向力 F_z との関係

また，構造別に比較を行った結果、Fig.9，Table 2 に示したように，電圧変化量の最大・最小値またその差に違いが生じていることがわかった．これは，導電粒子形状の違いにより導電経路の形成の仕方が異なるために，せん断変形による導通経路の分断の起こりやすさに違いが生じるため，電圧変化量 (ΔV) に違いが生じているものと考えられる．

同じ構造で感度の異なる感圧ゴム II では高感度の方が中感度に比べ，すべての値で大きな値を示していた．この為，高感度のゴムの方が電圧変化が生じやすいと考えられる．感度の違いはゴム内部の導電粒子の密度の違いにより生じており，その違いがせん断変形を加えた際の導通経路の分断量の違いとして現れ，電圧変化量の差となっていると考えられる．

5. まとめ

様々な種類や感度の感圧導電性ゴムの特性を調査する為，感圧導電性ゴムに法線方向力と接線方向力をそれぞれ加える実験を行なった．その結果，法線方向力を加えた場合の特性として，ヒステリシス特性，推移特性が存在することがわかった．このヒステリシス特性はゴムの種類によってその大きさが異なり，感度の違いでは大きな差異は見られなかった．また，これらの特性は感圧ゴムの種類・感度に依らず生じていることが明らかになった．

接線方向力を与えた場合の特性として，感圧導電性ゴムにせん断変形を与えると抵抗値が急激に上昇することがわかっており，今回の実験によってその変化量はせん断速度 ($\dot{\gamma}_s$) と法線方向力 (F_z) に依存していることが明らかになった．この特性は法線方向の特性と同様に感圧導電性ゴムの種類・感度に依らず生じていることがわかった．また，これに対し以下の関係式を求めた．

$$\dot{\gamma}_s = \sqrt[cF_z+d]{\frac{\Delta V}{aF_z + b}} \qquad (5)$$

この関係式を用いることで，電圧変化量 (ΔV) と法線方向力 (F_z) からせん断速度 ($\dot{\gamma}_s$) を推定することが可能になると考えられる．今後はこれらの特性を応用し，滑り覚センサを構成していく．

参考文献

[1] 多田泰徳，細田耕，浅田稔：" 内部に触覚受容器を持つ人間型柔軟指"，日本ロボット学会誌，Vol.23，No.4，pp.482-487，2005

[2] 石田豊, 近藤誠宏, 上田淳，" 滑り知覚を可能とする触覚センサを装着した多指ハンド" , 第 23 回日本ロボット学会学術講演会予稿集 2005,pp.1C14

[3] 藤本勲，山田陽滋，前野隆司，森園哲也，梅谷陽二：" PVDF フィルムを用いたヒトの指に学ぶ静摩擦覚を有するフィンガスキンの開発"，日本ロボット学会誌 Vol.22 No.6,pp806～814,2004

[4] 勅使河原，石川，下条，" CoP 触覚センサによる滑り検出～メカニズムの解明と被覆材の影響"，JSME ロボティクス・メカトロニクス講演会，pp.1A2-B09，2007

[5] 勅使河原誠一，石川正俊，下条誠：" 高速, 高感度な滑り覚センサの研究開発ー感圧導電性ゴムの特性ー"，ロボティクス・メカトロニクス講演会 2008,pp.1A1-H11

[6] 勅使河原誠一，西永知博，石川正俊，下条誠：" 滑り検出と感圧導電性ゴムの性質"，第 8 回計測自動制御学会　システムインテグレーション部門講演会 2007，pp.487-488

感圧導電性ゴムの特性を用いた滑り覚センサの研究開発
—抵抗値変化の高周波成分について—

High Sensitivity Slip Sensor utilizing Characteristics of Pressure Conductive Rubber
-High Frequency Components of Resistance Change-

○学　勅使河原 誠一（電通大）　学　清水 智（電通大）　正　多田隈 建二郎（電通大）
正　明 愛国（電通大）　正　石川 正俊（東京大）　正　下条 誠（電通大）

Seiichi Teshigawara (UEC), Satoru Shimizu (UEC), Kenjiro Tadakuma (UEC),
Aiguo Ming (UEC), Masatoshi Ishikawa (Univ. of Tokyo), Makoto Shimojo (UEC)

Slip detecting tactile sensors are essential to achieving a human-like gripping motion with a robot hand. Up until now, we have proposed flexible, thin and lightweight slip sensor utilizing characteristics of pressure conductive rubber. However, this sensor was difficult to distinguish between the object slip and the normal force change. So, we consider the separative method using high frequency components generated by object slip. In this paper, we will discuss about the high frequency components.

Key Words : Tactile Sensor, Slip Detection, Pressure conductive rubber

1.　はじめに

ロボットに人間のような五感を与える場合，視覚や聴覚についてはすでに実用的なセンサが開発されている．しかし，それだけでは人間の最大の特徴である道具を器用に扱うという行為をロボットを用いて実現することはできない．ロボットが人間の手の代わりになるような動作を行うためには，圧覚，滑り覚，温度覚などの情報を取得するための触覚センサが必要である．特に，物体の把持・操り動作を行うためには，滑り覚が重要な役割を果たす．そこで，これまでに歪ゲージや PVDF，カメラなどを用いた様々な滑り覚センサが開発されている [1][2]．検出手法はそれぞれ異なるが，物体の滑りが生じる直前の変化，すなわち“初期滑り”を検出するタイプのセンサが数多く報告されている．しかし，これらのセンサは構造が複雑であり，小型化・軽量化の問題がある．また，初期滑りによる出力変化と，物体との接触や法線力変化による出力変化との識別が困難である．本研究室においてもこれまで，薄型・柔軟な感圧導電性ゴムを用いた滑り覚センサを提案してきた [3]．しかし，従来型の滑り覚センサと同様，接触と初期滑りとの分離が困難であるという問題があった．そこで我々は，物体がセンサ表面を滑る直前に現れる複雑な抵抗値変化を利用することを検討している．本稿では，この複雑な出力変化について，周波数解析を行った結果を報告する．

2.　感圧導電性ゴム接線力付加実験

2.1　滑り覚センサの構成

本センサの構成を Fig.1 に示す．電極と感圧導電性ゴムを基本としており，電極は $1[k\Omega]$ の抵抗を介して $5[V]$ の電源に接続している．電極は，2 つが互い違いに渦を巻いた構造のものを用いている．この電極上に感圧導電性ゴム (6 [mm] × 6 [mm]) を乗せ，滑り覚センサを構成している．本センサは，ゴムを用いているため，柔軟・軽量・薄型 (0.5 [mm]) である．また，アンプ回路を必要とせず，非常に簡易な構成となっている．

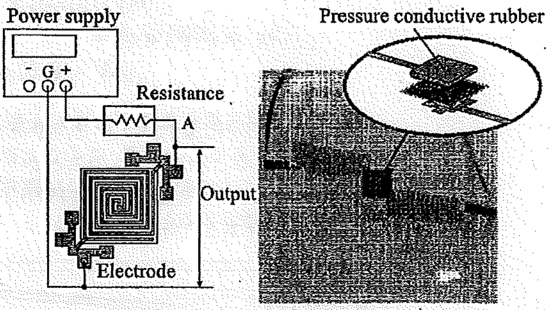

Fig.1 滑り覚センサの構成

2.2　接線力による抵抗値変化

Fig.2 の上段のグラフは，センサ上に置いた物体を水平方向に引張り，滑りを発生させたときの感圧導電性ゴムの抵抗値変化を示している．下段のグラフは，センサ表面に作用している力を示す．図中の縦線間の時刻において，物体の滑り変位が発生している．これより，ある一定の法線方向力を与えた状態で接線方向力が作用すると，低下していた抵抗値が増加することがわかる．また，物体の滑り変位が発生する直前において，非常に複雑な抵抗値変化が生じていることがわかる．

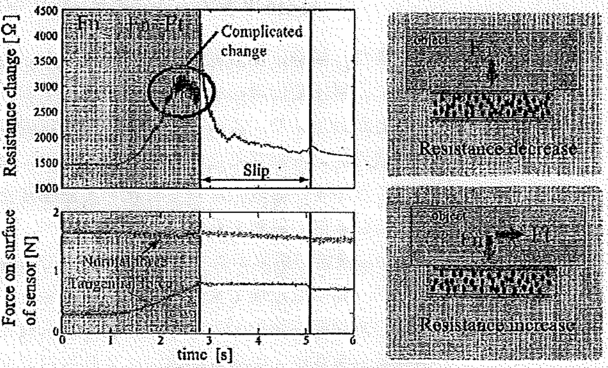

Fig.2 接線力が作用した際の抵抗値変化

3. 高周波成分の解析

前章に示したように，物体の滑り変位が発生する直前において，複雑な抵抗値変化が生じる．そこで，本章では，この複雑な変化に対してウェーブレット解析を行い，その周波数特性を調べる．さらに，法線方向力が変化した際の周波数成分との比較を行い，考察を行う．

本章で用いる実験装置の模式図を Fig.3 に示す．2.1 節で示した滑り覚センサを水平面上に配置し，この上にアクリルプレートをのせ，加圧子にて法線方向に荷重を加えた．加圧子を固定している自動ステージにて位置制御を行い，法線力を 2 $[N]$ に調節した．次に，挟みこんだアクリルプレートの端に糸を取り付け，ロードセルを介して自動ステージの動力によって引張り，センサ表面で滑らせた．アクリルプレートの滑り速度を $1[mm/s]$ に設定し，このときの電極間電位をサンプリングレート 10kHz で計測した．

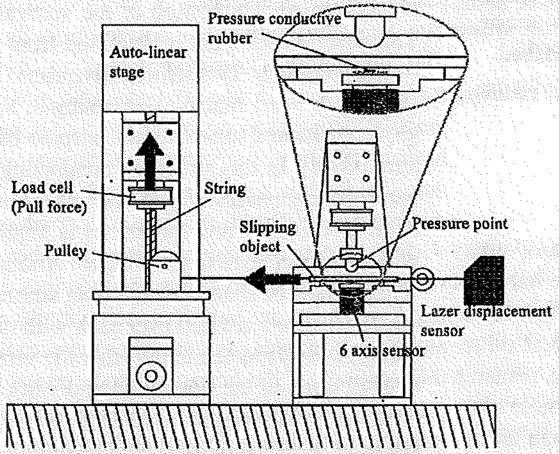

Fig.3 物体の滑り発生装置 (模式図)

以上のようにデータを計測し，これに対して連続ウェーブレット変換を行った結果を Fig.4 に示す．上段に示すグラフは，電極間電位変化であり，解析対象の信号である．本グラフの縦軸は電圧，横軸は時間である．下段のグラフは上段の電圧変化に対して連続ウェーブレット変換を行ったグラフである．縦軸は周波数に相当するスケール，横軸は時間である．縦軸の上方にいくほど低周波をあらわし，下方ほど高周波であることをあらわす．また，色の濃淡で強度を表している．本解析結果より，接線力付加による電圧変化が生じる初期においては，高周波成分はほとんど無く，強度も小さい．一方，プレートが滑り出す直前付近になると，高周波成分が増加し，1kHz 以上の高周波成分が現れた．物体が滑りだす初期において発生することから，これを用いることによって，初期滑りの検出が可能と思われる．

一方，接線力が作用した場合の周波数と法線力が変化した際の周波数を比較するため，センサ表面に対して垂直に負荷と除荷を行った場合の信号に対してウェーブレット解析を試みた．この電圧変化に対するウェーブレット解析の結果を Fig.5 に示す．負荷と除荷を行った際の周波数成分は最高でも，600[Hz] 程度であり，物体を滑らせたときに生じる高周波成分は現れなかった．以上より，滑りによって発生する周波数成分は，法線方向力変化によって生じる周波数成分よりも高いことが明らかになった．したがって，両者の周波数成分の違いを利用し，両者の分離が可能であると思われる．

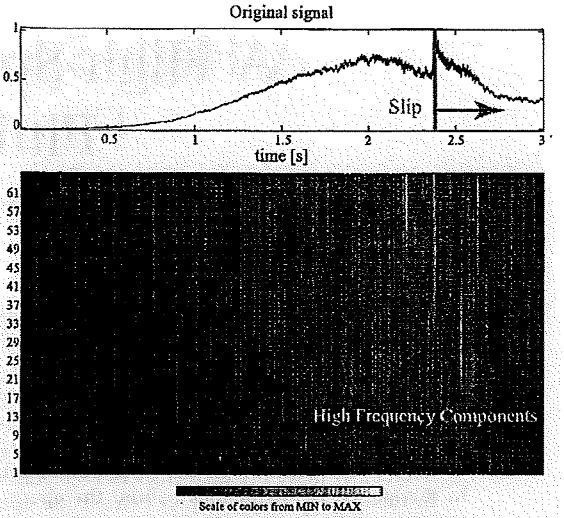

Fig.4 滑りが生じた際のウェーブレット解析結果

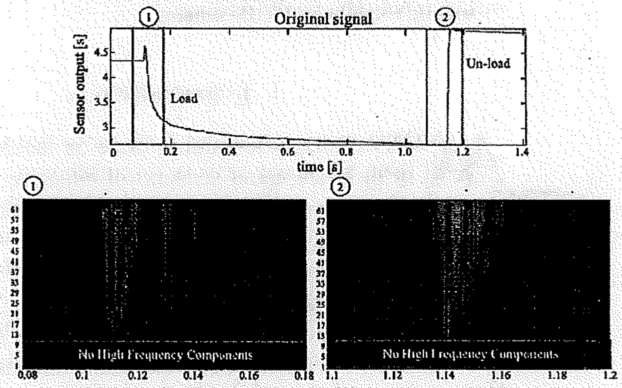

Fig.5 負荷と除荷を行った際のウェーブレット解析結果

4. まとめ

感圧導電性ゴムの特性を利用した滑り覚センサについて，法線力と滑りとの分離を行う手法について検討するために，物体の滑りが生じる直前に起こる複雑な抵抗値変化について周波数解析を試みた．その結果，その抵抗値変化には 1[kHz] 以上の高周波成分を多く含んでいることがわかった．また，法線力のみが付加された場合の出力変化についてもウェーブレット解析を行い，滑りが発生した場合の周波数成分を比較した．その結果，法線方向力が変化した際の周波数成分よりも，滑りが発生する際の周波数成分の方が高周波であることがわかった．以上より，この周波数成分の違いを利用することで，滑りと法線力変化との分離が可能と思われる．今後は，この高周波成分を利用した具体的な分離手法について検討していく．

参考文献

[1] 前野, 広光, 河合:"曲面状弾性フィンガの固着・滑り分布推定に基づく把持力の制御", 日本ロボット学会誌, vol.19,no.1,pp.91-99,2001

[2] A. Ikeda, Y. Kurita, J. Ueda, Y. Matsumoto, T. Ogasawara, *Grip force control for an elastic finger using vision-based incipient slip feedback*, IEEE/RSJ Int. Conf. on Intelligent Robots and Systems, pp.810-815, 2004

[3] 勅使河原, 明, 多田隈, 石川, 下条," 高速・高感度な滑り覚センサの研究開発", 第26回日本ロボット学会学術講演会 2008,pp.3L1-08

A High-Speed Mesh of Tactile Sensors Fitting Arbitrary Surfaces

Makoto Shimojo, Takuma Araki, Aigou Ming, *Member, IEEE*, and Masatoshi Ishikawa

***Abstract*—A tactile sensor is developed with the aim of covering a robot's entire structure, while reducing wiring requirement and ensuring high-speed response. The sensor detects the center point of load distribution on 2-D surfaces as well as the overall load. There are only four signal wires from the sensor. The sensor response time is nearly constant (within 1 ms) regardless of the number of detection elements, their placements or sensor areas. In this paper, the principles behind the operation of this sensor and the results of experiments using the sensor are described.**

***Index Terms*—High-speed response, mesh structure, reducing wiring, robot skin, tactile sensing.**

I. INTRODUCTION

AMONG many researches done on tactile sensors, many of them are about sensors for attaching to the hands of robots for the purpose of gripping and manipulating their hands [1], [2]. Recently, however, with the increased interest on research and development of robots in human-like form, research on the development of tactile sensors covering the whole body of the robot itself has become popular [3]–[5]. Although the applications for which these researches are intended do not require high spatial resolution of these sensors, they do require that the sensors be attachable to arbitrary surfaces that can cover a wide area. Moreover, rapid response is desired to ensure safety. Because these full body skin tactile sensors cover a wide area, the detection elements need to be spread over a wide range which in turn requires a lot of wiring for signal transmission. For this reason, when sensors are attached to movable parts such as the wrists and fingers, many problems occur from design limitations due to restrictions on movement imposed by the wirings [6]. Several studies have been done to solve these problems. We would like to introduce some of these attempts as follows.

First, tactile sensors have been developed by Inaba *et al.* where the number of wirings is the same as the number of detection elements [7]. This structure uses a mesh-structure spacer sandwiched between conductive sheets. When load is applied, the conductive sheets come into contact through the mesh to detect load. This developed sensor is flexible and can cover a wide area. However, the number of wirings increases as the area covered becomes larger.

Next, some tactile sensors have been developed with the matrix arrayed system. In this structure, the detection elements are placed on the intersection of the vertical and horizontal lines. The detection element is identified from the intersection of the row and column. This structure requires $(m+n)$ lines of wiring for an $(m \times n)$ matrix. For example, Seki *et al.* developed a glove-structured sensor for the purpose of measuring the grip of humans [8]. In this structure, conducting wires are sewn alternately along horizontal and vertical directions on pressure conductive rubber. While this sensor is flexible and durable, many wiring restricts free finger motion. Another type developed is a sensor made of sheets printed with stripes of pressure sensitive ink. Two sheets are laid over each with the stripes on one sheet along the horizontal and the other the vertical direction [9]. The intersections of the horizontal and vertical stripes serve as the pressure sensitive area. A stripe is as thin as about 0.1 mm, it is possible to realize high spatial resolution. However, the sensor is sheet like form, it is hard for the sensor to cover a curved surface.

Recently, a method called Electrical Impedance Tomography (EIT) was developed. Electrodes are arranged at the periphery of a conductive sheet. And the distribution of the resistance inside the conductive sheet is measured using inverse problem method [10]. Since there is no need for wiring inside the measurement area, the sensor can be made flexible, thin and extensible. However, on the other hand, a large number of electrodes may be needed to increase spatial resolution.

Other sensors developed uses serial bus as a way to reduce wiring. For example, Ohmura *et al.* proposed the reduction in the number of wirings by arranging a MPU (micro processing unit) on a sensor sheet with 32 pressure sensitive parts considered as a unit and combining high-speed serial buses of each sensor sheet [11]. However, scanning time problems results from the increase in number of elements. Other sensor types proposed are such as that: multiplexes the signal from the detection elements via spread spectrum transmission method [12], sequentially transmits the signal from detection elements through one line using delay circuitry [13]. Shinoda *et al.* proposed a very unique wireless technique through the use of a sensor chip whose transmission frequency changes with load. This sensor chips were dispersed under a flexible form that was formed to the desired shape, and transmission of power and signal is done through an external coil [14]. However, their development is now at a stage of the first trial prototype.

Manuscript received April 15, 2009; revised October 08, 2009; accepted October 08, 2009. Current version published March 10, 2010. The associate editor coordinating the review of this paper and approving it for publication was Prof. Evgeny Katz.

M. Shimojo, T. Araki, and A. Ming are with the Department of Mechanical Engineering and Intelligent Systems, University of Electro-Communications, Tokyo.182-8585 Japan (e-mail: shimojo@mce.uec.ac.jp; ming@mce.uec.ac.jp).

M. Ishikawa is with the Department of Information Physics and Computing, Graduate School of Information Science and Technology, University of Tokyo, Tokyo 113-8656, Japan (e-mail: ishikawa@k2.t.u-tokyo.ac.jp).

Digital Object Identifier 10.1109/JSEN.2009.2034982

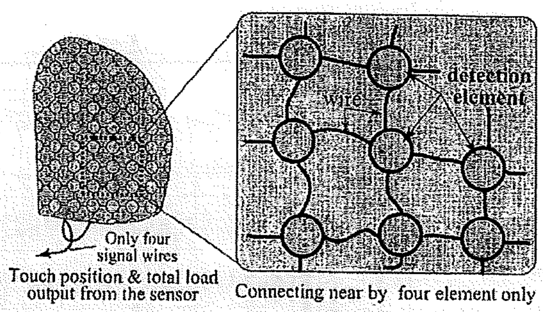

Fig. 1. Outline of the sensor. Net-like structure and only four output lines from the sensor.

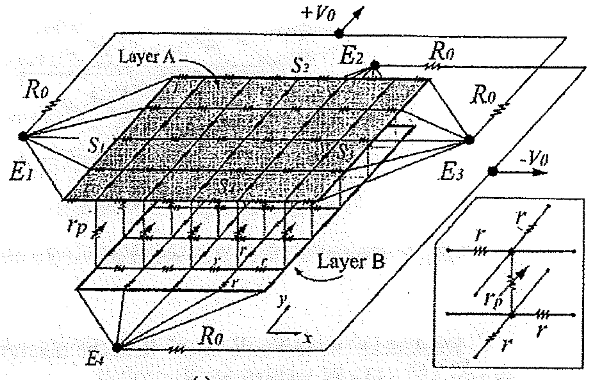

(a) (b)

Fig. 2. Structure of the sensor. A detector layer is sandwiched by $m \times n$ matrix arrayed resistor layers. (a) Three layered structure. (b) Detection element.

There are many other researches going on other than those mentioned above [15]. But these have a common problem described as follows.

1) Mounting on arbitrary surfaces: Many of the tactile sensors currently developed are of the sheet variety and cannot be mounted on arbitrary surfaces.
2) Excessive wiring: A lot of wiring are required for many detection elements when covering a wide area.
3) Sluggish response due to scanning: Since the number of detection elements becomes too many, scanning of every detection element results to delayed response time.

In this study, a mesh of tactile sensors that can be attached to arbitrary surfaces with reduced wiring requirement and rapid response was developed. The conceptual outline of the sensor is shown in Fig. 1. The sensor is formed into a structure resembling a net. It can be attached to arbitrary surfaces, and can detect the center of the load distribution as well as the overall load on 2-D surfaces. There are only four output lines from the sensor and internal connection is required only between adjacent detection elements. Moreover, since the sensor structure is analog circuit, the response speed is almost constant regardless of the number of detection elements, placement and surface area of the sensor. In summary, the sensor features the following.

1) Covers arbitrary surfaces: the sensor can be laid out like a net to cover arbitrary surfaces.
2) Reduced wiring: Lines from the sensor consist of four wires only regardless of number, surface area, or placement of detection elements.
3) High-speed response: Response time is less than 1 ms without regard to the number of detection elements which means that the sensor is adequate for use in control loops around 1 kHz; the standard used in robotics control.

II. SENSOR STRUCTURE

The structure of the sensor is shown in Fig. 2. As shown in this figure, the structure is a three-layered structure. Layer A is a $m \times n$ arrayed resistors. All resistors at the left end of layer A are connected to electrode E_1 which is connected to a voltage of $+V_0$ through the external resistor R_0. In like manner, all resistors at the right end are connected to the electrode E_3 and are connected to a voltage of $+V_0$. The network structure of layer B is the same as that of layer A. However, the electrode connections of layer B are found at the upper and lower ends unlike in the case of layer A. Layers A and B are connected by detection element r_p whose resistance varies with the load. Fig. 2(b) shows a unit element. The output of the sensor consists of the voltages from the four electrodes, E_1, E_2, E_3, E_4. The advantages gained from this kind of a structure are: 1) Sensor size can be varied easily by connecting any number of elements sequentially along the horizontal and vertical directions on the $m \times n$ matrix. 2) The unit detection element r_p can be replaced if the electrical resistance or electrical current changes with the physical value. For example, if a photo-reflector is used instead of pressure-conductive rubber, distance is detectable instead of force. That is, the sensor can be used easily not only as a 2-D load sensor but also as a 2-D proximity sensor. 3) Since the adjacent unit elements are connected into a net-structure, it is possible to cover arbitrary surfaces in the same way as covering an object with a net.

III. SENSOR PRINCIPLE

The detection element r_p changes its electrical resistance with load. When load is applied to the sensor, the value of the resistance r_p drops and the value of the electrical current increases. That is, in other words, the distribution of the load on the sensor is converted into the distribution of the electrical current flowing from layer A to layer B. For this sensor, the center of the load distribution can be detected as the center of the current distribution [16], [17].

A. Equivalent Circuit and Basic Equation

Fig. 3 shows the equivalent circuit at the neighborhood of a unit element. Current flowing from layer A to layer B through the resistor $r_p(i,j)$ is set to $I(i,j)$. The voltage $V_a(i,j)$ and $V_b(i,j)$ are the voltage of the corresponding nodes on layers A and B respectively. Applying Kirchhoff's current law on the layer A, the current flowing through the node indicated by the voltage $V_a(i,j)$ is equal to the current $I(i,j)$ passing through the resistor $r_p(i,j)$ as shown in Fig. 3. Thus, the following equation can be established:

$$\frac{1}{r}\{V_a(i-1,j) + V_a(i+1,j) + V_a(i,j-1) + V_a(i,j+1) - 4V_a(i,j)\} = I(i,j). \quad (1)$$

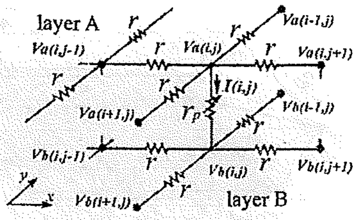

Fig. 3. Equivalent circuit at the neighborhood of a detection element.

Replacing the left side of (1) with the discrete Laplace operator ∇^2, (1) can be written as (2) [18]

$$\frac{1}{r}\nabla^2 V_a(i,j) = I(i,j). \tag{2}$$

Using the same method, the following equations can be derived for layer B:

$$\frac{1}{r}\nabla^2 V_b(i,j) = -I(i,j). \tag{3}$$

B. Position Coordinates of the Detector Element

Fig. 4 shows the position coordinate for the placement of a detector element. The detector elements are assumed to be distributed equally. Further, it is assumed that origin of $x_{i,j}$ falls on the center of the sensor. In order to satisfy these assumptions, $x_{i,j}$ is defined in (4), thus

$$x_{i,j} = \frac{2j-(n+1)}{n-1} \quad (-1 \le x_{i,j} \le +1). \tag{4}$$

Also, for y direction position coordinate $y_{i,j}$, set as defined in (5)

$$y_{i,j} = \frac{-2i+m+1}{m-1} \quad (-1 \le y_{i,j} \le +1). \tag{5}$$

In this manner of setting the coordinates, the placement of the detector elements form a matrix with uniform intervals and the position coordinates $x_{i,j}, y_{i,j}$ for all detector elements form an arithmetic progression. The Laplace operator then becomes zero as shown in (6)

$$\nabla^2 x_{i,j} = \nabla^2 y_{i,j} = 0. \tag{6}$$

This relationship will be used in Section III-D.

C. Boundary Conditions

Considering the electrical boundary conditions for the sensor shown in Fig. 4, the boundaries S_2 and S_4 of layer A do not have any external contact so that these layers are open terminals. Hence, no current flows from the outside and the voltage does not change. The boundary conditions therefore are shown, as in (7)

$$V_a(0,j) = V_a(1,j), \quad V_a(m+1,j) = V_a(m,j). \tag{7}$$

Next, let us consider the boundaries S_1 and S_3 for layer A which are connected to the electrodes E_1 and E_3, respectively, such that current flows in from the electrodes. This current passes through the externally connected resistor R_0. Hence, the value of this current can be determined from the voltage drop between the ends of R_0. Since the total of the currents that passes through the detector elements are equal to current that flows through R_0, (8) and (9) are established as follows:

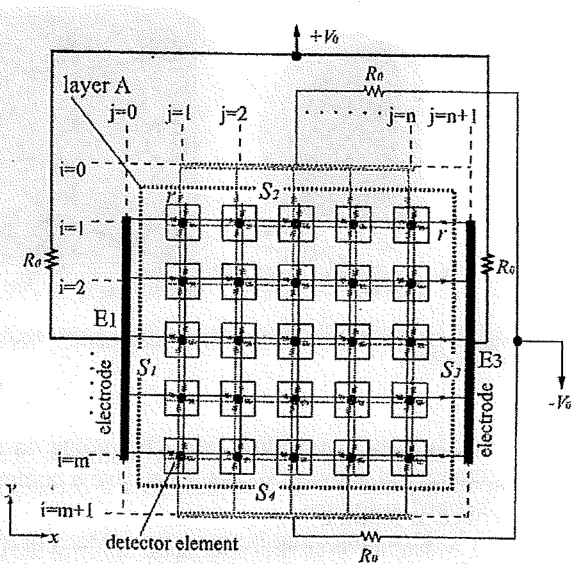

Fig. 4. Position of a detector element in layer A and electrical boundary conditions for the sensor.

$$\frac{1}{R_0}\{V_0 - V_{E1}\} = \frac{1}{r}\left\{\sum_{i=1}^{m}(V_{E1} - V_a(i,1))\right\} \tag{8}$$

$$\frac{1}{R_0}\{V_0 - V_{E3}\} = \frac{1}{r}\left\{\sum_{i=1}^{m}(V_{E3} - V_a(i,n))\right\}. \tag{9}$$

Further, since $j=0$ for electrode E_1 and $j=n+1$ for electrode E_3, the boundary conditions becomes as

$$V_a(i,0) = V_{E_1}, \quad V_a(i,n+1) = V_{E_3}. \tag{10}$$

Since layer B is similarly situated, the boundary conditions for this layer are similarly established, as in (7)–(10).

D. Total Current and Center of the Current Distribution

To determine the center of the distribution of the current value, it is necessary to determine the primary moment of current distribution with respect to the x direction. This primary moment I_x with respect to the x direction of the $m \times n$ matrix formed by the detector elements can be expressed as (11)

$$I_x = \sum_{i=1}^{m}\sum_{j=1}^{n} x_{i,j} I(i,j). \tag{11}$$

Replacing current $I(i,j)$ with (2) in the equation above gives (12) as follows:

$$I_x = \frac{1}{r}\sum_{i=1}^{m}\sum_{j=1}^{n} x_{i,j}\nabla^2 V_a(i,j). \tag{12}$$

Expanding the Laplace operator ∇^2 of (12) results to (13), which in turn can be expressed as in (14) with expanding and organizing it

$$\begin{aligned}I_x = \frac{1}{r}\Biggl\{&\sum_{i=1}^{m}\sum_{j=1}^{n} x_{i,j}V_a(i-1,j)\\ &+\sum_{i=1}^{m}\sum_{j=1}^{n} x_{i,j}V_a(i+1,j)\\ &+\sum_{i=1}^{m}\sum_{j=1}^{n} x_{i,j}V_a(i,j-1)\\ &+\sum_{i=1}^{m}\sum_{j=1}^{n} x_{i,j}V_a(i,j+1)-4\sum_{i=1}^{m}\sum_{j=1}^{n} x_{i,j}V_a(i,j)\Biggr\}\end{aligned} \tag{13}$$

$$\begin{aligned}I_x = \frac{1}{r}\Biggl\{&\sum_{i=1}^{m}\sum_{j=1}^{n} V_a(i,j)\nabla^2 x_{i,j}\\ &+\sum_{j=1}^{n}(x_{m,j}V_a(m+1,j)-x_{m+1,j}V_a(m,j))\\ &+\sum_{j=1}^{n}(x_{1,j}V_a(0,j)-x_{0,j}V_a(1,j))\\ &+\sum_{i=1}^{m}(x_{i,n}V_a(i,n+1)-x_{i,n+1}V_a(i,n))\\ &+\sum_{i=1}^{m}(x_{i,1}V_a(i,0)-x_{i,0}V_a(i,1))\Biggr\}.\end{aligned} \tag{14}$$

Next, let us apply the proper position coordinates and the boundary conditions to (14) and simplify the result. Firstly, the first item in (14) can be reduced to zero by applying the position coordinates settings defined by (6). Next, since $x_{i,j}$ is the function only for j, therefore, it is constant toward the direction of i, that is, $x_{m,j} = x_{m+1,j}$. With the boundary conditions given by (7), the second and third items of (14) become zero and (14) simplifies into the following equation:

$$\begin{aligned}I_x = \frac{1}{r}\Biggl\{&\sum_{i=1}^{n}(x_{i,n}V_a(i,n+1)-x_{i,n+1}V_a(i,n))\\ &+\sum_{i=1}^{n}(x_{i,1}V_a(i,0)-x_{i,0}V_a(i,1))\Biggr\}.\end{aligned} \tag{15}$$

Applying the boundary conditions given by (8) and (9) to (15) and imposing the boundary conditions given by (10) further results to (16) below

$$I_x = \frac{1}{n-1}\left(\frac{2m}{r}+\frac{n+1}{R_0}\right)\cdot(V_{E_1}-V_{E_3}). \tag{16}$$

In like manner, the primary moment I_y with respect to the y direction can be expressed in the following equation:

$$I_y = \frac{1}{m-1}\left(\frac{2n}{r}+\frac{m+1}{R_0}\right)\cdot(V_{E_2}-V_{E_4}). \tag{17}$$

Here, m, n, r and R_0 are constants. Hence, I_x can be computed as a constant multiplier of the voltage potential difference (E_1, E_3) between the electrodes of layer A. Similarly, I_y can be determined from the voltage potential difference (E_2, E_4) between the electrodes of layer B. Moreover, since the total current flowing from layer A to layer B is the current that flows through R_0, the total current I_{all} is given by (18)

$$\begin{aligned}I_{\text{all}} &= \sum_{i=1}^{m}\sum_{j=1}^{n} I(i,j)\\ &= \frac{2V_0 - V_{E_1} - V_{E_3}}{R_0} = \frac{2V_0 + V_{E_2} + V_{E_4}}{R_0}.\end{aligned} \tag{18}$$

With the above, the center of the current distribution defined as x_0 and y_0, can now be determined from (19)

$$x_0 = (I_x)/(I_{\text{all}}), y_0 = (I_y)/(I_{\text{all}}). \tag{19}$$

E. Numerical Modeling of the Load Distribution

The previous discussion established that the total current and the center of the current distribution can be determined from the voltage difference between the electrodes. In this section, we shall investigate the relationship between current $I(x, y)$ and the resistance of the pressure sensitive element $r_p(i, j)$. Let us consider layer A first. The current $I(x, y)$ flowing through $r_p(i, j)$ as shown in Fig. 3 can be expressed as (20)

$$I(i,j) = \frac{1}{r_p(i,j)}(V_a(i,j) - V_b(i,j)). \tag{20}$$

With this, (1) becomes

$$\begin{aligned}\left\{4+\frac{r}{r_p(i,j)}\right\}[V_a]_{i,j} - [V_a]_{i-1,j} - [V_a]_{i+1,j}&\\ -[V_a]_{i,j-1} - [V_a]_{i,j+1} - \frac{r}{r_p(i,j)}[V_b]_{i,j} &= 0.\end{aligned} \tag{21}$$

Next, let us consider the boundary conditions. From (8), and considering electrode E_1

$$\left(1+\frac{R_0}{r}m\right)V_{E1} = V_0 + \frac{R_0}{r}\sum_{i=1}^{m} V_a(i,1). \tag{22}$$

Similarly, from (9) and considering electrode E_3

$$\left(1+\frac{R_0}{r}m\right)V_{E3} = V_0 + \frac{R_0}{r}\sum_{i=1}^{m} V_a(i,n). \tag{23}$$

Equations similar to those for layer A can likewise be established for layer B. The equations for each point in layers A and B and the equations for each electrode E_1, E_2, E_3, and E_4 above, when taken altogether, form $(2mn+4)$ simultaneous equations. These equations serve as the numerical model for the sensor.

F. Total Load and Center of Load Distribution

In this section, the relationship between current $I(i, j)$ and load $F(i, j)$ is investigated. Let us suppose that, for this sensor, resistance r_p and load $F(i,j)$ are inversely related, as shown in (24)

$$r_p(i,j) = kF^{-1}(i,j) \tag{24}$$

where, k is a constant. Here, if the resistance r is much lower than resistance r_p ($r_p \gg r$), the voltage drop due to r would be very small. This means that we can say that the voltages at layers A and B, $V_a(i,j)$ and $V_b(i,j)$, are practically constant. Eq. (20) thus becomes (25)

$$I(i,j) = \frac{V_a(i,j) - V_b(i,j)}{r_p(i,j)} \approx \frac{V_A - V_B}{r_p(i,j)}. \tag{25}$$

From this, we can say that the current $I(i,j)$ and the load $F(i,j)$ are directly proportional as (26) indicates

$$I(i,j) = \frac{(V_A - V_B)}{k} F(i,j). \tag{26}$$

Consequently, the center of load distribution is the same as the center of the current distribution, x_0 and y_0 defined by (27) and (28)

$$x_0 = \frac{\sum_{i=1}^{m}\sum_{j=1}^{n} x_{i,j}F(i,j)}{\sum_{i=1}^{m}\sum_{j=1}^{n} F(i,j)} = \frac{I_x}{I_{\mathrm{all}}} \tag{27}$$

$$y_0 = \frac{\sum_{i=1}^{m}\sum_{j=1}^{n} y_{i,j}F(i,j)}{\sum_{i=1}^{m}\sum_{j=1}^{n} F(i,j)} = \frac{I_y}{I_{\mathrm{all}}}. \tag{28}$$

Moreover, since V_A and V_B are assumed to be practically constant, V_A is the average of V_{E1} and V_{E3}, while V_B is the average of V_{E2} and V_{E4}. Using these values, total load will be (29)

$$F_{\mathrm{all}} = \sum_{i=1}^{m}\sum_{j=1}^{n} F(i,j) \approx \frac{2kI_{\mathrm{all}}}{(V_{E1} + V_{E3} - V_{E2} - V_{E4})}. \tag{29}$$

IV. SIMULATION

The sensor consists of r, R_0 and r_p. Among them, r_p is decided from an actual detector. However, r and R_0 are parameters determined by the designer. Therefore, how r and R_0 affects the sensor characteristics is established from simulation.

A. Simulation Model

The numerical model of the sensor is made up of $(2mn+4)$ simultaneous algebraic equations established in Section III-E and shown in (30)

$$Sv = c. \tag{30}$$

Here, v represents the voltage, $V_a(i,j)$ and $V_b(i,j)$, respectively, and c represents the external applied voltage $\pm V_0$. Both are $(2nm+4)$ dimensional vectors. Moreover, S represents a $(2nm+4) \times (2nm+4)$ coefficient matrix. The value of S is determined from (21) with the boundary conditions defined by (22) and (23). The numerical solution to the equations of (30) was obtained using MATLAB.

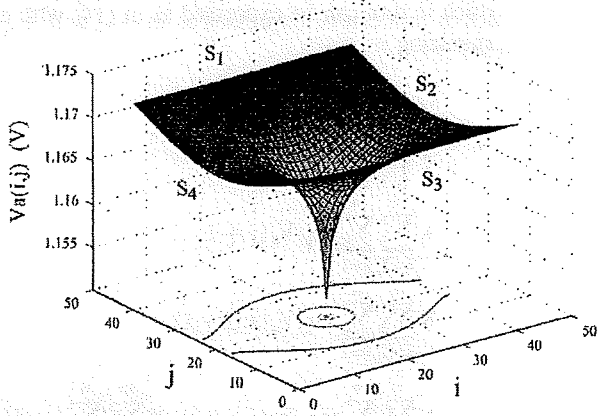

Fig. 5. Voltage $V_a(i,j)$ on the layer A with one point load. Elements are arranged in 41×41 grid, $V_0 = 15$ V, $R_0 = 10\mathrm{k}\,\Omega$, $r = 10\,\Omega$, $r_p = 864\,\Omega$ ($F_0 = 5$ N).

B. Effect of Network Resistance R

In this section, we will establish the relationship between the resistance r and sensor properties. First, let us look at an example of the simulation results for the voltage distribution in layer A shown in Fig. 5. In this case, a single load of $F_0 = 5$ N is applied at the center of the sensor. In the simulation, the voltage drop due to r is less than 0.02 V. It is very small.

In Section III-F, We suppose that resistance $r_p(i,j)$ and load $F(i,j)$ are inversely related and the resistance r is much lower than resistance r_p as shown in (31). Then, the center of load distribution is the same as the center of the current distribution, x_0 and y_0 defined by (27) and (28)

$$1 \gg r/r_p. \tag{31}$$

This assumption was verified by the simulation. Simulation was conducted with the values of r set at 10 Ω, 47 Ω, 100 Ω, and 150 Ω. The result is shown in Fig. 7. The figure clearly shows that when r increases, the voltage distribution of $V_a(i,j)$ changes. In Fig. 7, when r is 10 Ω, voltage $V_a(i,j)$ can be considered practically constant. However, as the value of r increases, the value of $V_a(i,j)$ tends to vary from a constant value. Also, although the polarity of voltage $V_b(i,j)$ is opposite to $V_a(i,j)$, the same changes occur in $V_b(i,j)$. As a result, the condition that $(V_a(i,j) - V_b(i,j))$ should be constant is no longer satisfied. It means that the current $I(i,j)$ and the load $F(i,j)$ are not proportional as (26) indicates. Therefore, it cannot be considered that the center of current distribution is the same as the center of load distribution.

Especially, this effect becomes a problem when multiple loads are applied on the sensor. As an example, Fig. 6 shows what happens when loads are applied on three points. It was assumed that the total of the loads on the three points is 5 N. As clearly shown in the figure, loading positions affected voltage distribution $V_a(i,j)$ so that $(V_a(i,j) - V_b(i,j))$ changed. This indicates that the location where load is applied affects the sensor output. The following section will investigate these effect.

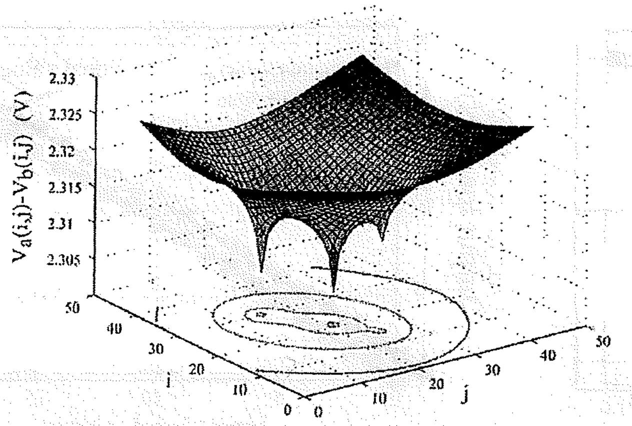

Fig. 6. Voltage of the $(V_a(i,j) - V_b(i,j))$ by the three-point load. Elements are arranged in 41×41 grid, $V_0 = 15$ V, $R_0 = 10k\ \Omega$, $r = 10\ \Omega$, Total load = 5 N.

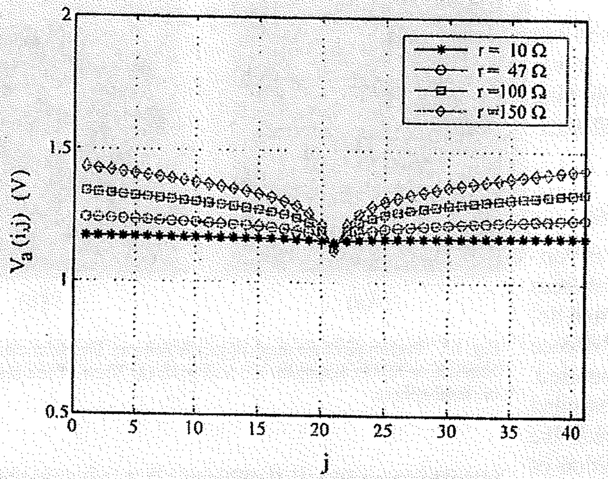

Fig. 7. Change of the $V_a(i,j)$ with resistance "r". Elements are arranged in 41×41 grid, $V_0 = 15$ V, $R_0 = 10\ \mathrm{k}\,\Omega, r_p = 864\ \Omega$ $(F_0 = 5$ N).

TABLE I
CHANGE OF r/r_p BY INPUT LOAD. ($k = 4320$ [N Ω])

load \ r	10 Ω	47 Ω	100 Ω	150 Ω
5 N	0.0115	0.0544	0.1157	0.1736
10 N	0.02315	0.01088	0.2315	0.3472
15 N	0.03472	0.1632	0.3472	0.5208
20 N	0.04630	0.2178	0.4629	0.6944

C. *Verification of Sensor Output Error*

The measurement error increases according to the increase in r. This is because the ratio r/r_p increased. However, when F increases, (24) states that r_p decrease. As a result, the ratio r/r_p increases. Table I shows the result of computing the ratio r/r_p when r_p is changed by input force F.

Hence, simulation was done to determine the measurement error when the load $F(i,j)$ and r are made to change. Simulation of the sensor output when the loads are applied on multiple points was conducted. Six loading points were considered in the simulation. The conditions in the simulation were, random load position with six loading positions and total loads of 5 N, 10 N, 15 N and 20 N. Moreover, the computations were done for values of r of 10 Ω, 47 Ω, 100 Ω, and 150 Ω. One-hundred computation runs per simulation condition were performed. The sensor error was shown by the average and standard deviations. Fig. 8 shows the position output error while Fig. 9 shows the total load error. The vertical axis of Fig. 8 represents the ratio of the position output error while that for Fig. 9 represents the ratio of the sensor output error for total load. Further, the horizontal axis for both figures represents the total load. It is clear that an error increases as total load increases. However, the results of the simulation described above show that for $r = 10\ \Omega$, the position error is within 0.5% while that for total load was within 2%. It means that this sensor operates with sufficient accuracy when r/r_p is less than 0.05.

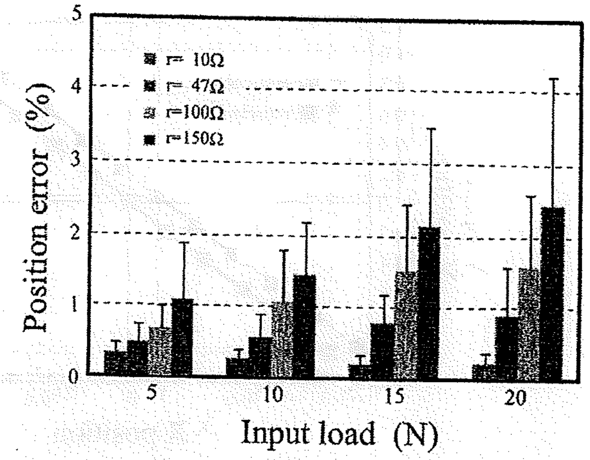

Fig. 8. The position output error by change of the total load. Elements are arranged in 41×41 grid, $V_0 = 15$ V, $R_0 = 10$ k Ω, loading point: random, number of loading = 6.

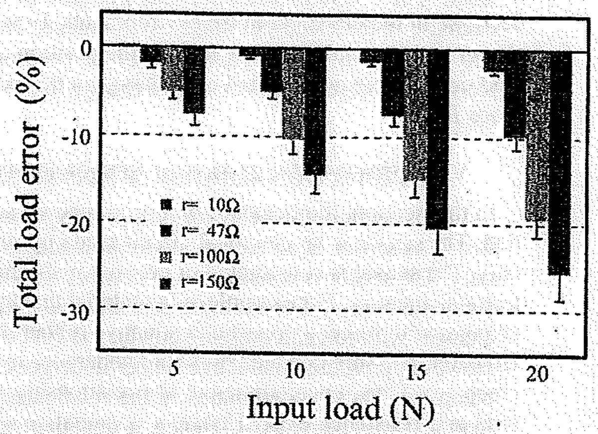

Fig. 9. The total load output error by change of the total load. Elements are arranged in 41×41 grid, $V_0 = 15$ V, $R_0 = 10$ k Ω, loading point: random, number of loading = 6.

D. *Effect of Resistance* $r0$

It is clear from sensor structure shown in Fig. 2 that as R_0 increases, the total current I_{all} decreases. At the same time, the voltage drop due to R_0 increases, thus the voltage of $(V_a(i,j) - V_b(i,j))$ becomes smaller. At the same, the voltage differences between electrodes, $(V_{E_1} - V_{E_3})$ and $(V_{E_2} - V_{E_4})$, become

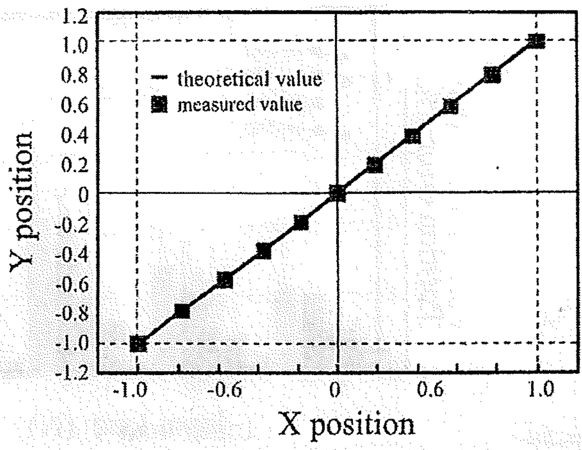

Fig. 10. Experimental result of the position output by two-point load.

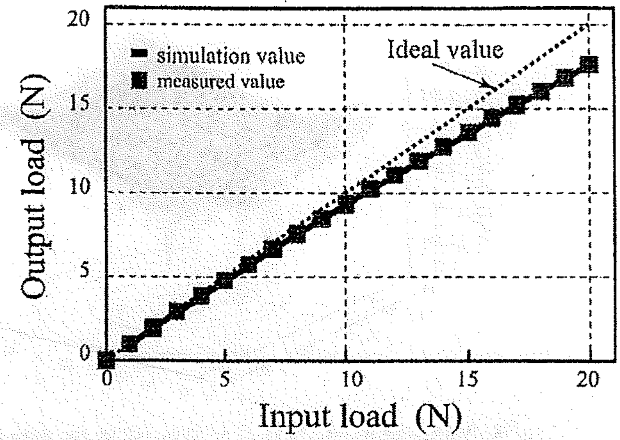

Fig. 11. Experimental result of the total load output by two-point load.

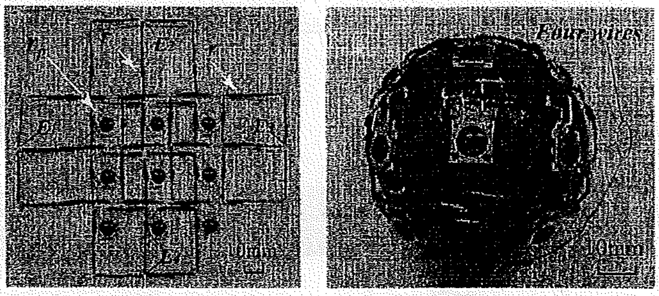

(a) (b)

Fig. 12. Prototype of the mesh of tactile sensors. Detector elements are pressure conductive rubber arranged in 3 × 3 grid. (a) View of the sensor. (b) Attached on semi-sphere.

small. These results mean that the S/N ratio of the sensor will decrease in the electrical noise environments. However, it was shown in this simulation that error of the position and the total load output were not affected by a change in the external resistance R_0.

V. PROTOTYPE VALIDATION OF SENSOR PROPERTIES

In this section, the behavior of a prototype sensor was verified. The sensor is an electrical circuit made up of resistances only. The sensor is constructed of network resistance r and detector element r_p. For example, as a material that the resistance changes with force, a pressure conductive rubber may be used. However, pressure conductive rubber undergoes hysteresis and creep etc. Thus, uncertainties in the relationship between the load and resistance exist. Hence, a quantitative evaluation of this sensor is difficult. For this reason, adjustable resistors were used as detector element r_p. In the experiment, elements were arranged in 5 × 5 grid. The circuit constants were assigned as: $r = 47\ \Omega$ and $R_0 = 10\ \text{k}\ \Omega$. Moreover, the load and resistance r_p were assumed to satisfy the relationship defined by (24), and k was set to 4320 [N Ω].

A. Position Measuring Experiment

The sensor is able to detect the center of the load distribution. A validation experiment was conducted on the position output under two point loading. The sensor outputs the center position of the load distribution. First of all, loads F_1 and F_2 were applied at the sensor coordinate positions $(-1.0, -1.0)$ and $(+1.0, +1.0)$. Then the sensor position output was measured. In the experiment, the sum $F_1 + F_2 = 10$ N was fixed. F_1 was made to change from 0 N to 10 N with 1 N-increments. Hence, the sensor position output must be changed by steps from $(-1.0, -1.0)$ to $(+1.0, +1.0)$. The results of the experiment are shown in Fig. 10. With an increase in load, the sensor output correctly moved the straight lines connecting the load positions. The figure shows that the simulation results and the measured values agree very well.

B. Load Measurement Experiment

The sensor also can be used to output the total value of the distributed loads. Two loads, F_1 and F_2, were applied on the coordinate positions $(0, 0)$ and $(+0.5, +0.5)$ and the sensor load outputs were measured. During the experiment, $(F = F_1 = F_2)$ and F was made to vary from 0 N to 10 N with 0.5 N-increments. The results of the experiment are shown in Fig. 11. The figure shows that the simulation results and the measured values agree very well. However, Fig. 11 also clearly shows that as the load increases, the measured values departed from the ideal values. This difference is the influence of the two load which affected each other, as shown in Fig. 6.

VI. SENSOR PROTOTYPE USING PRESSURE CONDUCTIVE RUBBER

Fig. 12 shows the prototype of a sensor. The prototype sensor used a pressure-conductive rubber manufactured by Inaba Rubber Company, Ltd., as the detector element r_p. The elements were arranged in a 3 × 3 grid. The resistance r was set to $r = 47\ \Omega$. As the sensor has a net-structure, it can be mounted on a sphere as shown in Fig. 12(b).

A. Response to Impulse Load

The sensor was tested to measure the time of the response. The experiment was conducted to apply an input load on the sensor by an Impulse Hammer (Ono sokki, GK-300) and to measure the time until the sensor outputs a constant voltage corresponding to the input position. Fig. 13 shows the time response of the position output just after the input load is applied. As

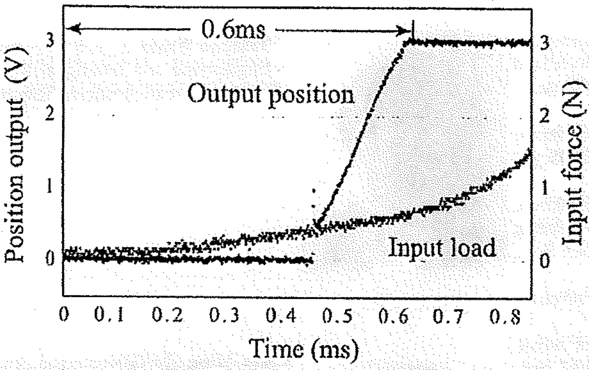

Fig. 13. Time response of the position output just after the input load is applied.

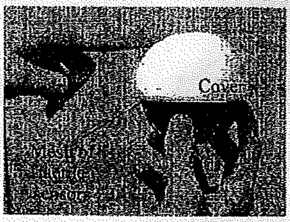

Fig. 14. Photograph of the stroking experiment with sensor covered by styrene foam.

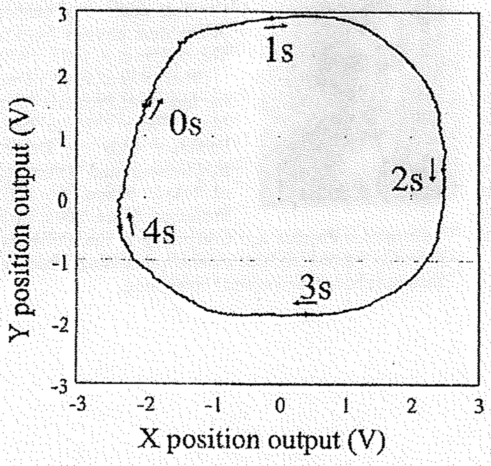

Fig. 15. A locus of the sensor's position output. The cover top is pushed by a fingertip drawing a circle.

shown in the figure, it took about 0.6 ms to output the input position after the load is applied. In general, the sensor feedback control cycle is 1 ms or less. The sensor is adequate for use in control loops around 1 kHz; the standard used in robotics control.

B. Semi-Spherical Surface Attachment Experiment

Fig. 14 shows detector elements arranged on a semi-spherical surface and these elements were covered by a semi-spherical styrofoam [19]. Fig. 15 shows the sensor output when the cover top is pushed so that a circle may be drawn by a fingertip. It can be seen from the figure that a neat locus is formed. Even when the elements are arranged discretely, the output can be obtained continuously through the use of a cover serving as sensor's skin.

VII. SUMMARY

A mesh of tactile sensors is developed with the aim of covering a robot's entire structure, while reducing wiring requirement and ensuring high-speed response. The sensor has a net-structure, can cover arbitrary surfaces and can detect the center of load distribution applied to 2-D surfaces as well as the total load. The wirings of numerous detection elements are connected only to adjacent elements such that there are only four output signal lines from the sensor. Further, the sensor, regardless of the number of elements, placement, and sensor area, the speeds of response were practically constant (within 1 ms). In this study, the sensor principle was explained and the prototypes were made. The basic characteristics defining the sensors were shown in the experiment results on position detection, load detection, and response characteristics.

ACKNOWLEDGMENT

We wish to express our thanks to Inaba Rubber Company, Ltd., for providing us with the prototype of the detector element. We wish to thank Dr. Carson Reynolds for valuable advice.

REFERENCES

[1] H. R. Nicholls and M. H. Lee, "A survey of robot tactile sensing technology," *Int. J. Robotics Res.*, vol. 8, no. 3, pp. 3–30, 1989.
[2] M. H. Lee and H. R. Nicholls, "Tactile sensing for mechatronics—A state of the art survey," *Mechatronics*, vol. 9, pp. 1–31, 1999.
[3] V. J. Lumelsky, M. S. Shur, and S. Wagner, "Sensitive skin," *IEEE Sensors J.*, vol. 1, no. 1, pp. 41–51, Jan. 2001.
[4] H. Iwata and S. Sugano, "Whole-body covering tactile interface for human robot coordination," in *Proc. IEEE Int. Conf. Robot. Autom.*, 2002, vol. 4, pp. 3818–3824.
[5] T. Mukai, M. Onishi, T. Odashima, S. Hirano, and Z. Luo, "Development of the tactile sensor system of a human-interactive robot "RI-MAN"," *IEEE Trans. Robotics*, vol. 24, no. 2, pp. 505–512, Apr. 2008.
[6] M. Shimojo, A. Namiki, M. Ishikawa, R. Makino, and K. Mabuchi, "A tactile sensor sheet using pressure conductive rubber with electrical-wires stitched method," *IEEE Sensors J.*, vol. 5, no. 4, pp. 589–596, 2004.
[7] M. Inaba, Y. Hoshino, K. Nagasaka, T. Ninomiya, S. Kagami, and H. Inoue, "A full-body tactile sensor suit using electrically conductive fabric and strings," in *Proc. IEEE/RSJ Int. Conf. Intell. Robot. Syst.*, 1996, pp. 450–457.
[8] K. Seki, M. Shimojo, S. Sato, and A. Takahashi, "Development of a grasping pressure distribution sensor with high flexibility," *Trans. SICE*, vol. 31, no. 9, pp. 1528–1530, 1995.
[9] TekscanInc. [Online]. Available: http://www.tekscan.com/
[10] A. Nagakubo, H. Alirezaei, and Y. Kuniyoshi, "A tactile distribution sensor based on inverse problem theory," *J. Robot. Soc. Jpn.*, vol. 25, no. 6, pp. 162–171, 2007.
[11] Y. Ohmura, Y. Kuniyoshi, and A. Nagakubo, "Conformable and scalable tactile sensor skin for curved surfaces," in *Proc. IEEE Int. Conf. Robot. Autom.*, 2006, pp. 1348–1353.
[12] Y. Yamada, K. Yamamoto, N. Tsuchida, and M. Komai, "A transmission system for multiplex sensor signals using spread spectrum systems with synchronization tracking method," *J. Robot. Soc. Jpn.*, vol. 7, no. 1, pp. 11–18, 1989.
[13] M. Nilsson, "Tactile sensors and other distributed sensors with minimal wiring complexity," *IEEE/ASME Trans. Mechatronics*, vol. 5, no. 3, pp. 253–257, Sep. 2000.
[14] M. Hakozaki, H. Oasa, and H. Shinoda, "Telemetric robot skin," in *Proc. IEEE Int. Conf. Robot. Autom.*, 1992, vol. 2, pp. 957–961.

[15] H. Kawaguchi. T. Someya, T. Sekitani, and T. Sakurai, "Cut-and-paste customization of organic FET integrated circuit and its application to electronic artificial skin," *IEEE J. Solid-State Circuits*, vol. 40, no. 1, pp. 177–185, Jan. 2005.

[16] M. Shimojo, T. Araki, A. Ming, and M. Ishikawa, "A ZMP sensor for a biped robot," in *Proc. IEEE Int. Conf. Robot. Autom.*, 2005, pp. 1200–1205.

[17] M. Shimojo, T. Araki, S. Teshigawara, A. Ming, and M. Ishikawa, "A net-structure tactile sensor covering arbitrary surface and ensuring high-speed response," in *Proc. IEEE/RSJ Int. Conf. Intell. Robot. Syst.*, 2007, pp. 670–675.

[18] , A. L. Bovik, Ed., *Handbook of Image and Video Processing*, 2nd ed. New York: Elsevier, 2005, pp. 543–545.

[19] M. Shimojo, "Mechanical filtering effect of elastic cover for tactile sensor," *IEEE Trans. Robot. Autom.*, vol. 13, no. 1, pp. 128–132, Feb. 1997.

Makoto Shimojo received the B.E. degree in mechanical engineering from the University of Electro-Communications, Tokyo, Japan, in 1973, the M.E. Eng. degree from the Tokyo Institute of Technology, Tokyo, in 1976, and the Dr. Eng. degree from the University of Electro-Communications in 1993.

From 1976 to 1992, he was a Senior Researcher at Industrial Products Research Institute, Tsukuba, Japan. From 1993 to 1997, he was a Senior Researcher at the National Institute of Bioscience and Human Technology, Tsukuba. From 1985 to 1986, he was a Visiting Scholar at Stanford University, Stanford, CA. From 1997 to 2001, he was a Professor of Computer and Information Sciences at Ibaraki University. Since April 2001, he has been a Professor of Mechanical Engineering and Intelligent Systems at the University of Electro-Communications. His current research interests include mechatronics, tactile sensing system, and human interface using tactile information.

Prof. Shimojo is a Fellow of the Japan Society of Mechanical Engineers.

Takuma Araki is with Department of Mechanical Engineering and Intelligent Systems, University of Electro-Communications, Tokyo, Japan.

Aiguo Ming (M'02) received the B.E. degree in mechanical engineering from Hunan University, Hunan, China, in 1983, the M.E. degree in precision engineering from Yamanashi University, Yamanashi, Japan, in 1987, and the Dr. Eng. degree in precision engineering from the University of Tokyo, Tokyo, in 1990.

From 1990 to 1991, he was with Mitutoyo Corporation, Tokyo. From 1991 to 1994, he was a Research Associate with the Department of Mechanical Systems, Yamanashi University. Since 1994, he has been an Assistant Professor and then Associate Professor with the Department of Mechanical Engineering and Intelligent Systems, University of Electro-Communications. His current research interests include robotics and development of mechatronic systems.

Masatoshi Ishikawa received the B.E., M.E., and Dr. Eng. degrees in mathematical engineering and information physics from the University of Tokyo, Tokyo, Japan, in 1977, 1979, and 1988, respectively.

From 1979 to 1989, he was a Senior Researcher at the Industrial Products Research Institute, Tsukuba, Japan. From 1989 to 1999, he was an Associate Professor with the Department of Mathematical Engineering and Information Physics, University of Tokyo, where, from 1999 to 2001, he was a Professor. Since 2001, he has been a Professor of Information Physics and Computing at the University of Tokyo. His current research interests include parallel processing, smart sensor, vision chip, sensor fusion, robotics, and optical computing.

2009 IEEE International Conference on Robotics and Automation
Kobe International Conference Center
Kobe, Japan, May 12-17, 2009

Skillful Manipulation Based on High-speed Sensory-Motor Fusion

Taku Senoo, Yuji Yamakawa, Satoru Mizusawa, Akio Namiki, Masatoshi Ishikawa and Makoto Shimojo

Abstract—**This video introduces the demonstration of skillful manipulation using a high-speed robot system. The system consists of visual and tactile sensors at a rate of 1 kHz and a high-speed hand-arm manipulator. The high-speed sensory-motor fusion improves not just the speed of existing robot manipulations, but robotic skills by introducing the features peculiar to high-speed motion. Based on such a concept, new variations of skillful manipulation were achieved.**

I. INTRODUCTION

In recent years, many robotic manipulation systems have been developed. However such systems were designed with a primary goal of the emulation of human capabilities, and less attention to pursuing of the upper limit in terms of speed for mechanical systems.

To achieve such dynamic fast motion, we have developed a high-speed manipulation system. This system consists of a multi-fingered hand with tactile sensors, a wire-drive arm, and a stereo active vision system. The cycle time of sensor feedback and control processing is set at 1ms. Therefore the robot can react quickly to target motion in unpredictable conditions.

Moreover new strategies for high-speed manipulation are developed utilizing the feature of high-speed motion. Several tasks show that high-speed active control enables stable and robust manipulation. In addition such a high-speed control strategy can be applied to various complicated manipulation. This result indicates that high-speed manipulation improves robotic skills.

II. SYSTEM CONFIGURATION

A. *Motor System*

The hand [1] consists of three fingers and a wrist. It has 10-DOF in total. A small harmonic drive gear and a high-power mini actuator are fitted in each finger link. The design of this actuator is based on the new concept that maximum power output, rather than rated power output, should be improved. The hand can close its joints at 180 [deg] per 0.1 [s]. Its maximum velocity is 300 [rpm], and the maximum output is 12 [N].

The arm is a wire-drive manipulator (Barrett Technology Inc.). The manipulator has 4-DOF consisting of alternately revolution and bending motion. High-speed movement with maximum velocity of the end-effector of 6 [m/s] and maximum acceleration of 58 [m/s^2] is achieved.

The hand-arm system is shown in Fig.1 (a).

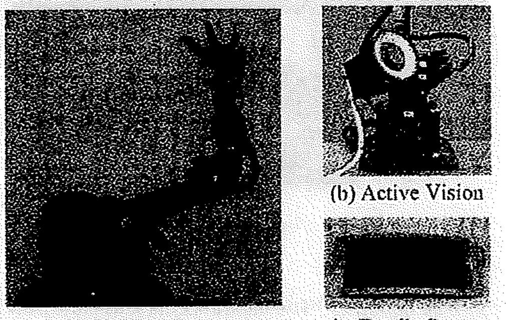

(a) Hand-Arm System

(b) Active Vision

(c) Tactile Sensor

Fig. 1. System configuration

B. *Sensory System*

Figure 1 (b) shows a column parallel vision system (CPV) [2] mounted on the 2-DOF (tilt, and pan) active mechanism. The CPV has 128×128 pixel photo detectors and an all pixel parallel processing array. Various visual processing (moment detection, segmentation and so on) are achieved within 1 ms because execution is in parallel.

The tactile sensor [3] is a sheet-like object as shown in Fig.1 (c). The sensor consists of the two outer electrically conductive films and the inner pressure-conductive rubber. The sensor can measure the center position of a two dimensional distributed load and the total load within 1 ms. The sensor is attached to the top link of each finger.

III. SKILLFUL MANIPULATION

A. *High-speed Manipulation*

A high-speed robot system improves not just the speed of existing robot manipulations. Pursuing the upper limit in terms of manipulation speed, we have developed appropriate new control for high-speed manipulation. Here stable and robust manipulation by introducing the features peculiar to high-speed motion are presented as shown in Fig.2.

1) Dribbling: The hand dribbles a small ball between two fingers [4]. The dribbling period is around 100 ms. In this task, new concept called "dynamic holding" is proposed. This means that high-speed active control enables the maintaining of periodically stable motion. Through dynamic holding states, there is an increasing possibility that novel transition of contact state is achieved.

T. Senoo, Y. Yamakawa, S. Mizusawa and M. Ishikawa are with Dept. of Creative Informatics, Graduate School of Information Science and Technology, University of Tokyo, 7-3-1 Hongo, Bunkyo-ku, Tokyo 113-8656, Japan. `Taku_Seno@ipc.i.u-tokyo.ac.jp`

A. Namiki is with Dept. of Mechanical Engineering, Graduate School of Engineering, Chiba University, 1-33 Yayoi-cho Inage-ku Chiba-shi, Chiba 263-8522, Japan. `namiki@faculty.chiba-u.jp`

M. Shimojo is with the Dept. of Mechanical Engineering and Intelligent Systems, Univ. of Electro-Communications, 1-5-1 Chofugaoka, Chofu-shi, Tokyo 182-8585, Japan. `shimojo@mce.uec.ac.jp`

978-1-4244-2789-5/09/$25.00 ©2009 IEEE

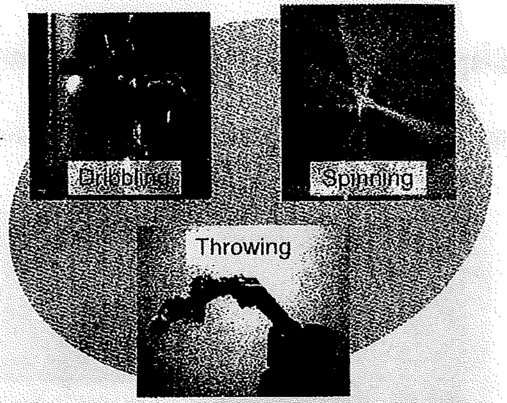

Fig. 2. High-speed manipulation

2) Pen Spinning: The hand repeats alternately the rotation of a pen-shaped object using left and center fingers and using right and center fingers [5]. The spinning strategy is based on the feature that rotational motion is stable when its speed is fast. Moreover the contact force and the timing of shifts about the axis of rotation are controlled in real-time by tactile feedback.

3) Throwing: The hand-arm manipulator throws a ball towards the target [6]. The release control with three fingers is designed so that the error of the ball direction is reduced using the apparent force, which is generated by high-speed arm swing. In order to achieve high-speed arm swing a kinetic chain algorithm is also presented, which is a mechanism to explosively radiate kinetic energy.

B. Complicated Manipulation

Such new control strategies for high-speed manipulation can be expanded to more complicated manipulations. We achieved skillful handling of more practical objects as shown in Fig.3.

1) Knotting of a Rope: Manipulation of flexible objects with robotic hands is a difficult issue. We have challenged to knot a rope as a simple example [7]. By high-speed sensory feedback control, the hand can dexterously control a flexible object regardless of its unpredictable moiton. Moreover a new strategy of motion for robot hands corresponding to mathematical elements of knot theory is presented.

2) Grasping with Tweezers: Considering robots work in human society, it is important for robot hands to handle a typical human tool. We achieved grasping a rice grain and a screw with tweezers [8]. High-speed visual servoing enables the control of force between a finger and a tool in real-time. This result means that a robot hand can handle many objects of various sizes with a tool.

3) Dynamic Regrasping: A new type of regrasping using high-speed performance is developed [9]. The dynamic regrasping consists of throwing and catching unlike with previous one while keeping a contact state. We achieved dynamic regrasping for objects of which mass distribution is not uniform and different-shaped objects.

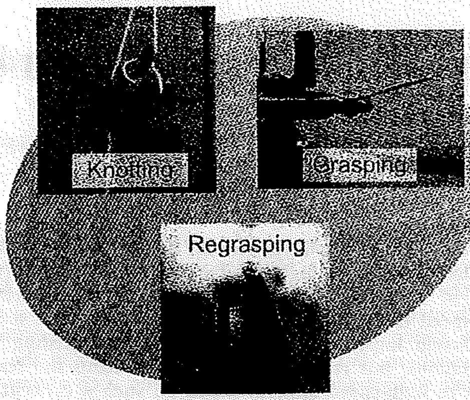

Fig. 3. Complicated manipulation

IV. CONCLUSIONS

These videos show that high-speed sensory-motor fusion has great potential to produce new control strategies and new robotic skills. Integrating high-speed dynamic manipulation as shown in this video and conventional static manipulation, more suitable robotic work for practical use would be realized.

These experimental results and other manipulations are shown on the web site [10].

REFERENCES

[1] A. Namiki and Y. Imai and M. Ishikawa and M. Kaneko, *Development of a High-speed Multifingered Hand System and Its Application to Catching*, IEEE/RSJ Proc. of Int. Conf. on Intelligent Robots and Systems, pp.2666-2671, 2003.

[2] Y. Nakabo, M. Ishikawa, H. Toyoda and S. Mizuno, *1ms Column Parallel Vision System and It's Application of High Speed Target Tracking*, Proc. of IEEE Int. Conf. on Robotics and Automation, pp.650-655, 2000.

[3] M. Shimojo, A. Namiki, M. Ishikawa, R. Makino and K. Mabuchi, *A Tactile Sensor Sheet Using Pressure Conductive Rubber With Electrical-Wires Stitched Method*, IEEE Sensors Journal, Vol.4, No.5, pp.589-596, 2004.

[4] D. Shiokata, A. Namiki and M. Ishikawa, *Dynamic Dribbling Using a High-speed Multifingered Hand and a High-speed Vision System*, IEEE/RSJ Proc. of Int. Conf. on Intelligent Robots and Systems, pp.3945-3950, 2005.

[5] T. Ishihara, A. Namiki, M. Ishikawa and M. Shimojo, *Dynamic Pen Spinning Using a High-speed Multifingered Hand with High-speed Tactile Sensor*, IEEE/RSJ Proc. of Int. Conf. on Humanoids, pp.258-263, 2006.

[6] T. Senoo, A. Namiki and M. Ishikawa, *High-speed Throwing Motion Based on Kinetic Chain Approach*, IEEE/RSJ Proc. of Int. Conf. on Intelligent Robots and Systems, pp.3206-3211, 2008.

[7] Y. Yamakawa, A. Namiki, M. Ishikawa and M. Shimojo, *Knotting Manipulation of a Flexible Rope by a Multifingered Hand System based on Skill Synthesis*, IEEE/RSJ Proc. of Int. Conf. on Intelligent Robots and Systems, pp.2691-2696, 2008.

[8] S. Mizusawa, A. Namiki and M. Ishikawa, *Tweezers Type Tool Manipulation by a Multifingered Hand Using a High-speed Visual Servoing*, IEEE/RSJ Proc. of Int. Conf. on Intelligent Robots and Systems, pp.2709-2714, 2008.

[9] N. Furukawa, A. Namiki, T. Senoo and M. Ishikawa, *Dynamic Regrasping Using a High-speed Multifingered Hand and a High-speed Vision System*, Proc. of IEEE Int. Conf. on Robotics and Automation, pp.181-187, 2006.

[10] http://www.k2.t.u-tokyo.ac.jp/fusion/index-e.html

Paper:

High Speed and High Sensitivity Slip Sensor Utilizing Characteristics of Conductive Rubber

–Relationship Between Shear Deformation of Conductive Rubber and Resistance Change–

Seiichi Teshigawara*, Kenjiro Tadakuma*, Aiguo Ming*,
Masatoshi Ishikawa, and Makoto Shimojo***

*Department of Mechanical Engineering and Intelligent Systems, The University of Electro-Communications
1-5-1 Chofugaoka, Chofu, Tokyo 182-8585, Japan
E-mail: teshigawara@rm.mce.uec.ac.jp
**Department of Mathematical Engineering and Information Physics, Faculty of Engineering, The University of Tokyo
7-3-1 Hongo, Bunkyo-ku, Tokyo 113-0033, Japan

[Received October 20, 2008; accepted January 17, 2009]

Humans can grasp an object without information such as a coefficient of friction or weight. To implement this grasping motion with the robot hand, sensors have been proposed that detect an incipient slip within the contact surface or stick-slip. A large number of slip sensors have been proposed, but small, flexible, and practical slip sensors are currently not available yet. We have been involved in research and development activities for a center of pressure (CoP) tactile sensor that is small and flexible. This sensor uses a pressure conductive rubber to detect the central position of the load distribution and total load. As a result of using the sensor to make experiments on slip detection, we found that a peculiar change appeared in the load output of the sensor immediately before the slip displacement of an object occurred. Based on this output change, we proposed a control method that was capable of setting a grasping force in accordance with the weight of an object. However, the principle was not made clear that caused the output change to occur. We hypothesized that the change was caused by the characteristics of the pressure conductive rubber used for the material of the sensor. As a result of making verification experiments based on this hypothesis, we found that the output change was due to a change in the resistance value when the pressure conductive rubber shear deformed. It was also found that the scale of a change in the resistance value was dependent largely upon the shear deformation speed of the pressure conductive rubber. This paper describes the principle that a peculiar change occurs in the CoP sensor immediately before the occurrence of an object slip. It also reports the characteristics of the pressure conductive rubber that have newly been made apparent.

Keywords: slip detection, pressure conductive rubber, tactile sensor

1. Introduction

A tactile sensor that collects information such as contact force, slip, and temperature senses is needed for a robot to take action in such a way that it works instead of the human hand. Particularly, if the robot grasps an object of which weight is unknown, puts the grasped object on the table smoothly on the table, or delivers it to someone, the slip sense plays an important role. For this reason a variety of slip sensors have been proposed.

Johansson et al. [1, 2] researched human grasping motion and clarified that humans grasped an object with the minimum grasping force causing a slip to occur. They also showed a partial slip is important between the skin and the grasped object. A partial slip is the one that occurs between an object within the contact surface and the skin surface. It is said that the slip displacement of an object is generated by the extended area of a partial slip and then its transition to the entire slip. If a partial slip is detected that occurs immediately before its transition to the entire slip, an object can be grasped with the minimum grasping force and without slipping it off. Trembley et al. [3] proposed a slip sensor detecting this partial slip at the first time. They placed two acceleration sensors in a spherical silicon rubber with projections called the "nib" to develop a sensor that detected vibration when a partial slip occurred on the surface of the sensor. Howe et al. [4] placed four PVDF films in a semi-cylindrical silicon rubber to develop a sensor that detected vibration when a partial slip occurred on the surface of the sensor. Maeno et al. [5] modeled the structure of the human finger tissue by using the infinite element method in addition to the perception of Johansson et al. to clarify the nature of an individual tactile receptor. They simulated a human grasping method to develop a sensor with strain gauges arranged within a curved elastic body at certain intervals [6, 7]. This indicated it possible to detect a partial slip and grasp an object whose weight and coefficient of friction are unknown. Ikeda et al. [8] proposed a method to use a camera to observe the surface of contact between an elastic body and a rigid plate and presume a slip tolerance. As described above, the detection methods are different, but many research and development activities are reported for such sensors that detect a change immediately before the slip of an object, that is, an "incipient slip."

On the other hand, we propose a method that utilizes a sensor detecting the load of a tangential force generating an object to slip to increase a grasping force before a slip displacement occurs in an object and prevent it from slipping [9]. This method employs the 2-dimensional CoP sensor developed by our laboratory. We have experimentally confirmed the characteristics that if an object is slipped on the CoP sensor, the load output drops immediately before the slip displacement of the object and that if the slip displacement occurs, the load output returns to its original level. The sensor uses these characteristics to detect a change immediately before a slip occurs [10]. We have proven that this method is capable of grasping an object with a proper grasping force and almost no slip displacement even if the weight of an object is different. The method has also succeeded in grasping a cup whose weight changes on the way (**Fig. 1**).

Reference [9] does not clarify the principle that slip of an object causes a change to occur in the load output of the CoP sensor. In this paper, Section 2 briefly describes the principle of the CoP sensor and a change in the load output due to a slip. In Section 3, we use a simple configuration consisting of electrodes and a pressure conductive rubber to make an experiment that an object is slipped on the silicon rubber surface and then describes the principle that a change occurs in the load output of the CoP sensor. Section 4 discusses an experiment that investigated the characteristics of a change in the resistance value for the shear deformation of the pressure conductive rubber and that reports the characteristics of the rubber that have been made apparent.

2. Load Output Change of CoP Sensor

The CoP sensor is structured in such a way that a pressure conductive rubber (made by Inaba Rubber Co.) is sandwiched between two conductive films on layers A and B [12]. It is capable of detecting the central position of the load distribution and the total load. It is characterized mainly by flexibility, thinning, lightweight, wire saving, and high-speed responsiveness within 1 ms.

Reference [10] made an experiment that the CoP sensor was mounted on a cylinder simulating the fingertip of the robot hand to grasp an object with a certain force and slip it vertically downwards. The model of this experiment is illustrated in the left of **Fig. 2**. We measured a normal force and a tangential force (tensile force of an object) by using the load cell to compare a change in the output of the CoP sensor with the actual force working on the surface of the sensor. As a result, almost no change was found in the normal force from immediately before and after the object slipped. However, it was found that the load output of the CoP sensor significantly decreased (area graph-circled in **Fig. 2**). As the CoP sensor is a sensor to detect the load in the normal direction, such an output change cannot usually be thought to occur. On the other hand, compared with the tangential force, the timing of a decrease in the load output of the CoP sensor is coincident with that of the tangential force to act. This implies that the tangential force was added to cause some change in the sensor, resulting in such a change as above. The next section examines the cause of this output change.

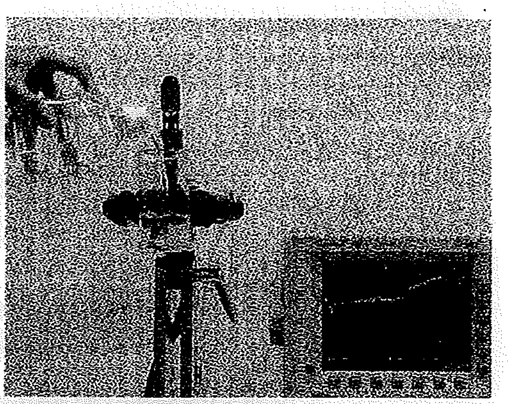

Fig. 1. Grasping force control for the object whose weight change (pouring water into a cup).

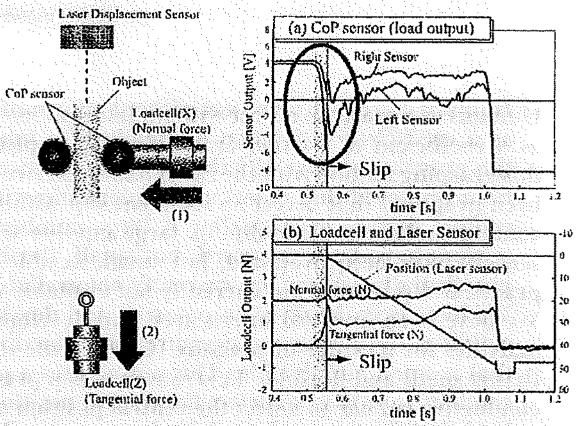

Fig. 2. Result of slip detection experiment using CoP tactile sensor.

3. Load Output Change in CoP Sensor and Resistance Change in Pressure Conductive Rubber

From the principle, a load output change in the CoP sensor is dependent upon a resistance change in the pressure conductive rubber. It is presumed that the deformation of the pressure conductive rubber occurring when an object slips causes its resistance to change. In the con-